Fermi National Accelerator Laboratory

FERMILAB-Pub-95/132
Revised

The APM Bright Galaxy Catalogue

J. Loveday

Fermi National Accelerator Laboratory
P.O. Box 500, Batavia, Illinois 60510

Operated by Universities Research Association Inc. under Contract No. DE-AC02-76CHO3000 with the United States Department of Energy

Disclaimer

The APM Bright Galaxy Catalogue

Jon Loveday

Fermi National Accelerator Laboratory,
PO Box 500, Batavia,
Illinois 60510, USA.

loveday@fnal.gov

Revised August 23, 1995

Abstract

The APM Bright Galaxy Catalogue lists positions, magnitudes, shapes and morphological types for 14,681 galaxies brighter than b_J magnitude 16.44 over a 4,180 square degree area of the southern sky. Galaxy and stellar images have been located from glass copy plates of the United Kingdom Schmidt Telescope (UKST) IIIaJ sky survey using the Automated Photographic Measuring (APM) facility in Cambridge, England. The majority of stellar images are rejected by the regularity of their image surface brightness profiles. Remaining images are inspected by eye on film copies of the survey material and classed as stellar, multiple stellar, galaxy, merger or noise. Galaxies are further classified as elliptical, lenticular, spiral, irregular or uncertain. The 180 survey fields are put onto a uniform photometric system by comparing the magnitudes of galaxies in the overlap regions between neighbouring plates. The magnitude zero-point, photometric uniformity and photographic saturation are checked with CCD photometry. Finally, the completeness and reliability of the catalogue is assessed using various internal tests and by comparing with several independently constructed galaxy catalogues.

Key words: catalogues — galaxies: fundamental parameters — galaxies: general — galaxies: photometry.

1 Introduction

The APM Galaxy Survey (Maddox *et al.* 1990a, b) includes about two million galaxies down to magnitude $b_J = 20.5$ over 4300 square degrees of the southern sky. It was the first machine-generated galaxy survey to cover an area of sky significantly larger than one Schmidt plate, and has proved an important survey for measuring galaxy number-magnitude counts over a wide magnitude range (Maddox *et al.* 1990c) and particularly for the most reliable measurement to-date of the angular correlation function of galaxies on large scales (Maddox *et al.* 1990d). This latter measurement was one of the first results to rule out the standard cold dark matter model of galaxy formation (eg. Davis *et al.* 1985).

Unfortunately, the APM Galaxy Survey, while complete to a faint magnitude limit of $b_J = 20.5$, is not very reliable for galaxies brighter than $b_J \approx 16.5$. There are several reasons for this. Firstly,

the surface density of galaxies brighter than $b_J \approx 16.5$ is only about 1/20 of the surface density of stars at the same magnitude limit even at the galactic poles. Therefore the selection of an uncontaminated bright galaxy sample requires an exceptionally reliable method of rejecting stars and merged images. Secondly, photographic emulsions have a limited dynamic range, and in order to detect images as faint as $b_J = 20.5$, the brighter images are necessarily saturated. Thirdly, bright stars have diffraction spikes and 'ghost' images (UKSTU handbook) and large galaxies contain substructure. All of these factors prevent the standard APM image parameters, which were designed to classify small, faint images, from selecting a sufficiently reliable bright galaxy catalogue.

This paper describes the construction of a bright galaxy catalogue, complete to $b_J = 16.44$, using the same APM scans used for the faint survey. We developed a semi-automated method of star-galaxy separation, whereby most stellar images were rejected (losing only about 3% of galaxies) and the remaining images inspected by eye on a film copy of the photographic plate. The distinction is emphasized between a survey *constructed* by eye, for example the Zwicky *et al.* (1961-68) catalogue or the Lick (Shane and Wirtanen 1967) survey, where the observer has to locate each image and *then* decide whether it should be included in the catalogue, and a semi-automated survey like the present one where the observer is given the position of each image satisfying a magnitude limit, and then classifies it as a galaxy or star. It is much easier for the eye to distinguish a galaxy from a star than it is to select a complete magnitude or diameter limited sample, and so the semi-automated survey should be much more reliable.

The APM Bright Galaxy Catalogue (APM-BGC) covers almost the same area as the faint APM galaxy survey of Maddox *et al.* (1990a, b), including 180 out of the 185 fields of the fainter survey, an area of approximately 4,180 square degrees. Figure 1 shows the distribution of the 180 survey fields in an equal area projection on the sky.

The construction of the present catalogue was first described by Loveday (1989). A similar survey has been carried out by Raychaudhury (1989) in the region towards the 'Great Attractor', and there is an ongoing effort (Raychaudhury *et al.* 1994) to map out the galaxy distribution near the equator.

The layout of the paper is as follows. The construction of the bright galaxy catalogue, including star-galaxy separation and plate matching, is described in Section 2. Internal tests for uniformity, completeness and consistency are described in Section 3 and comparison with other catalogues is made in Section 4. Section 5 describes the CCD calibrations used to check the APM to b_J magnitude conversion, as a further test of photometric uniformity in the survey, and to define a second-order correction for photographic saturation. In Section 6 we describe the catalogue data and present plots of the galaxy distribution. We compare the angular and spatial correlation functions of early and late type galaxies in the APM-BGC in Section 7. Finally, the properties of the catalogue are summarized in Section 8.

2 Construction of the Catalogue

2.1 The APM Measurements

The Automated Plate Measuring (APM) machine in Cambridge is a high-speed laser microdensitometer with on-line image detection and processing. Technical details are given by Kibblewhite *et al.* (1984) and by Maddox (1988). Plate scanning occurs in two passes—firstly the sky background is

measured in 640×640 0.5mm (33.6 arcsec) square pixels over the plate, with images being removed by median filtering. Note that if a galaxy image occupies a substantial fraction of a sky pixel, then the sky will be biased high in that pixel and hence the flux from that and nearby galaxies will be underestimated. This could cause us to bias against low surface brightness galaxies. We plan to investigate this possible bias using simulations in a future paper.

In the second pass, images are detected as connected groups of pixels with densities higher than a set threshold above local sky, determined from bilinear interpolation of the background map. Each image is parameterized by fifteen numbers: integrated isophotal density D; x and y coordinates on the plate measured in 8μ units; three second-order moments σ_{xx}, σ_{xy} and σ_{yy}; peak density; and finally an areal profile—the image area A_i above eight density levels $D_i = t + 2^{(i-1)}$, where i runs from 1 to 8. The threshold t was set at twice the *rms* noise in the measured sky, and corresponds to a surface brightness of $\mu_J \approx 24.5 - 25 b_J$ mag arcsec^{-2} (Maddox *et al.* 1990a). The APM magnitude m is defined as $+2.5 \lg D$, and so is reversed in sign from usual magnitude systems. A rough conversion, accurate to ≈ 0.5 mag, from m to b_J for $b_J \lesssim 17$ is given by $b_J \approx 29 - m$. This zero-point differs from that for faint images due to mild saturation of the brighter galaxies.

2.2 Star-Galaxy Separation

For twelve of the survey plates, a 90×90 pixel raster scan was made, using the APM machine, around the 4000 brightest images on each plate. Displaying each raster scan in turn enabled rapid classification of these images. Unfortunately, constraints on the amount of APM scanning time available meant that only a small fraction of the survey plates could be scanned in this way. Therefore, a semi-automated method for separating stars from galaxies, using just the standard APM image parameters described above, was devised and is described in this subsection.

In the faint survey (Maddox *et al.* 1990a), areal profile information (the 'ψ-classifier') is used to discriminate galaxy from stellar and noise images on each survey plate. The quantity ψ is defined as

$$\psi = 1000 \lg \left(\sum_{i=1}^{10} w_i(m)[p_i(m) - p_i^*(m)]^2 \right), \qquad (1)$$

where p_i is the ith areal profile for $i = 1 \ldots 8$, the peak density for $i = 9$ and the radius of gyration for $i = 10$. For each parameter p_i, a scatter plot against magnitude m is produced, and the stellar locus $p_i^*(m)$ is located as a function of magnitude. For each image the difference between the parameter p_i and the stellar locus $p_i^*(m)$ at the appropriate magnitude is calculated for all i. The differences from each p_i are summed in quadrature with a set of weighting factors w_i, equal to the reciprocal of the estimated variance in p_i.

For objects in the magnitude range $17 < b_J < 20.5$, selecting images with $\psi > 1000$ yields a galaxy sample that is $\approx 95\%$ complete and with $< 10\%$ contamination from stellar and merged stellar images. For brighter objects the number of stars relative to the number of galaxies becomes very large and so a ψ-selected galaxy sample will suffer from an unacceptable rate of contamination.

At $b_J \approx 16$, the best galaxy sample that can be selected using the ψ parameter has $> 50\%$ contamination from stars and merged images, although many of the merged objects can be identified using an additional two parameters based on the radius of gyration and the fraction of saturated image area (Maddox *et al.* 1990a). Use of the 'k' and 'μ' parameters reduces merger contamination

to $\sim 5\%$ at $b_J \approx 17$.

For such bright objects, the APM parameterization no longer contains all the information available from the UKST plates. The stars display haloes and diffraction spikes, and galaxies have detailed sub-structure. Also, both stars and galaxies are saturated. Therefore we used areal profile information in conjunction with visual inspection of photographic plate copies in order to select a more reliable bright galaxy sample.

The 3000 or so images with $m > 12.0$ ($b_J \lesssim 17.0$) on each plate from the scans of Maddox *et al.* (1990a,b) are sorted by density and binned with twenty objects per bin. Stellar profiles cluster closely around the median for each bin as $\approx 95\%$ of images with $b_J \leq 16.5$ are stars. Since galaxies are resolved, extended objects, they have a broader profile and thus stand out from the stars. Figure 2 shows areal profiles for (a) 10% of stars and (b) all galaxies in the APM magnitude range 12.5–12.6 on one plate. The median area is calculated at each profile level in each magnitude bin. Twenty objects per bin is a good compromise between having a small density range per bin but therefore only a few images to determine the median, and having wider bins giving a less noisy median but wider scatter about the median.

We define the 'profile residual error' (PRE), ε_j, for image j by

$$\varepsilon_j = \langle A^1_{m(j)} \rangle^z \sum_{i=1}^{8} \frac{|A^i_j - \langle A^i_{m(j)} \rangle|^x}{\langle A^i_{m(j)} \rangle^y}. \qquad (2)$$

Here A^i_j is the area at the ith profile level for image j and $\langle A^i_{m(j)} \rangle$ the median area at the ith profile level for j's magnitude bin. The denominator $\langle A^i_{m(j)} \rangle^y$ gives extra weight to higher profile levels, where there is smaller area. This is desirable since at low surface brightness levels haloes around bright stars often resemble galaxies, it is only towards the brighter core of the stellar image that bright stellar profiles become regular. The factor $\langle A^1_{m(j)} \rangle^z$ scales each PRE by the median isophotal area for that magnitude bin to the power z, since one expects large images, having more pixels, to suffer less from Poisson noise. This definition of profile residual error is more general than the ψ classifier (equation 1) used for the faint survey (Maddox 1988, Maddox *et al.* 1990a) and allows a better star/galaxy separation for bright images to be achieved. Choice of the parameters x, y, z is discussed below.

The raster scan classifications proved to be very valuable for calibrating the performance of the PRE in separating stars from galaxies. Figure 3 plots the profile residual error ε against APM magnitude for one field. The dashed horizontal line marks the PRE cutoff used for rejecting stars and the symbols show image classifications made from the raster scans. It is clear from Figure 3, that even using the customized PRE parameter, visual checking of some images is unavoidable to obtain a $\gtrsim 95\%$ complete galaxy sample with less than 5% stellar contamination.

It was decided to aim for a galaxy sample with 97% completeness and with negligible stellar contamination by rejecting obvious stars with a low value of ε and then inspecting the remaining images on a film copy of the plate. The weighting powers x, y, z were adjusted to minimize the number of images N_{eye} that needed to be inspected to obtain a completeness of 97% for the twelve plates which had been pre-classified from raster scans. The optimal values of x, y, z were found to be $x = 1.00$, $y = 2.14$, $z = 0.675$. By minimizing N_{eye} for each of the twelve rastered fields separately, the parameters x, y, z were found to have standard deviations of 0.2, 0.4 and 0.2 respectively. Using these parameters required all images with $\varepsilon > 2.05 \times 10^{-2}$, an average of 539 objects for each of these

twelve plates, to be inspected to obtain 97% completeness. An aimed completeness of 98% would have required an average of 665 objects to be inspected on each plate. As well as taking about 20% longer, nearly all of the additional images would be stars, and the 'tedium factor' of checking so many stars might actually cause more galaxies to be missed.

There is a danger that plate-to-plate variations in ε (*e.g.* due to differences in seeing) could give rise to changes in completeness, but this should be unimportant since we identify only about 125 galaxies per plate down to $b_J \approx 16.5$, and so a change in completeness of 3% would have a much smaller effect on the number of identified galaxies than Poisson fluctuations in the galaxy density.

2.3 Plate Eyeballing

2.3.1 Masking Large Images

Images larger than 1–2mm in diameter cause problems since they are often either removed by the APM machine or split up into many sub-images. In order to understand why the APM machine removes large images, some understanding of the way in which APM scanning is carried out is necessary. Note that since the plates for this survey were scanned, the APM hardware has been upgraded which completely avoids the problem. The following description refers to the operation of the APM machine when the APM-BGC survey was being carried out.

The APM machine scans the plate in 3 areas—horizontal strips across the top, middle and bottom of the plate. Each area is scanned in 2mm columns, each of which overlaps the previous column by 1mm, so that nearly every part of the plate is scanned twice, in addition to the preliminary background scan. The pixel locations and densities above the threshold in each column are stored in memory so that they can be merged with adjoining pixels in the subsequent column. Due to available memory constraints, image pixels cannot be stored for more than one column, and so any group of pixels spanning more than two scan columns is dropped from the image list. Thus all images larger than 2mm in horizontal extent are lost, and those larger than 1mm will be lost if they happen to span three columns. As an example, the dense central region of a globular cluster will often be removed, leaving an annulus of tightly-packed images marking the outer regions of the cluster. Also, large images will of course obscure any galaxies lying behind them. Thus regions around large images were 'drilled' out of the survey as follows.

A grey-scale plot of the APM background map was made for each field and compared with a film copy of the plate. Any large images and bad satellite trails were marked on the plot. The same background map was then displayed on an image display and the vertices of parallelogram-shaped holes defined interactively. Parallelograms were chosen to enable satellite trails to be removed, although in practice these trails rarely showed up on the background maps and most holes drilled were rectangular. A file of hole coordinates was saved, with typically ten holes drilled per plate.

2.3.2 Image Classification

All objects brighter than $m = 12.0$, an average of 3124 images per plate, were extracted from $\sim 300,000$ images detected by each scan. The profile residual error ε (equation 2) was calculated for each of these bright images. Areas around large images were drilled out as described above, and

a plate-scale finding chart marking objects brighter than $m = 12.5$ and with PRE $\varepsilon > 2.05 \times 10^{-2}$, 425 objects per plate when averaged over the whole survey, was made. By placing the finding chart under a film copy of the plate, these objects were inspected with a magnifying lens and assigned a 1 digit classification code as shown in Table 1. Blended images were only placed into class 8 when stellar and galactic components were of comparable intensity as judged by eye. Most large galaxies contain one or two faint stellar images which were ignored in this classification scheme. An average of 124 objects per plate (*i.e.* about 30% of those inspected) were classified as a galaxy, and eyeballing each plate took about two hours.

2.4 Plate Matching

It is important for statistical studies of galaxy clustering that a catalogue be uniform, or at least have a known selection function, over its whole area. Due to slight variations in observing, processing and scanning conditions, the magnitudes measured from different plates for the same object can vary by about ± 0.5 mag. (Fig. 5 below). Galaxies in the plate overlap regions were therefore used to match the plates onto a common magnitude system.

Since the field centres are separated by 5°, and the APM scans cover the full $6° \times 6°$ area of the UKST plates, there is an overlap of about $6° \times 1°$ between neighbouring plates. The 180 eyeballed survey plates give rise to 493 overlaps, with an average of twelve galaxies in each overlap. Only galaxies were used in the overlap comparisons since stars brighter than $b_J \approx 16.5$ are very badly saturated on UKST J-plates. These galaxies are used to calculate a magnitude zero-point offset between each pair of plates. An iterative algorithm (Maddox 1988, Maddox *et al.* 1990b) is then used to find the set of additive plate corrections most consistent with the overlap zero-point offsets. Figure 4 plots magnitude difference against mean magnitude for each matched pair of overlap galaxies (a) before and (b) after plate matching. The matching procedure reduces the *rms* magnitude difference from 0.28 to 0.18, and since there are an average of twelve galaxies per overlap, the *rms* error in zero point per overlap $\approx 0.18/\sqrt{12} \approx 0.05$ mag. Thus whereas plate matching in the faint survey, with about 3000 galaxies per overlap, is dominated by systematic errors of order 0.03 mag in the field corrections, here we are dominated by random errors in individual galaxy magnitudes. (The following section suggests that field-effects, which could give rise to systematic errors, are negligible.) We do not use the corrections from the faint survey since most bright galaxies are affected by saturation, and some plates are more saturated than others.

Figure 5 is a histogram of plate corrections found by the matching procedure. The distribution is roughly Gaussian with $\sigma \approx 0.2$. Since the eyeballed samples were limited to a fixed APM magnitude limit before matching, the shallowest fields after matching were up to 0.5 mag brighter than the mean. Although many fields were eyeballed to a much fainter limit, a complete sample could be obtained only by limiting to the matched magnitude limit of the shallowest field, $m_{mat} = 12.9$. The number of galaxies to this limit was only 6250, and so a second pass was made, eyeballing those survey plates with a matched magnitude limit shallower than $m_{mat} = 12.5$ down to this limit. The plate matching was then repeated as the larger number of overlap galaxies changes the field zero-points slightly. An error in the matching procedure (due to too many iterations) was subsequently discovered (Loveday 1989), resulting in the magnitude limit of the shallowest field being $m = 12.63$. After this second pass, 14681 out of 23747 eyeballed galaxies satisfied the matched magnitude limit $m_{mat} = 12.63$. An equal-area plot of the final plate zero-point corrections is shown in Figure 6.

3 Internal Tests for Uniformity, Completeness and Classification Consistency

3.1 Field Effects

In any wide-field telescope such as a Schmidt one expects vignetting towards the field edges, and indeed this can be seen on the plates. The APM machine partially corrects for this by on-line background subtraction. Maddox *et al.* (1990b) have discussed in detail why vignetting is still a problem for faint images. Basically, vignetting decreases the slope of the measured density *vs.* flux relation so that images measured in vignetted regions of the plate are analyzed at a higher threshold than those near the centre. For brighter images, threshold effects become negligible and for saturated images vignetting can actually increase the measured magnitude. This is because saturation density is roughly constant over the whole plate, *i.e.* independent of vignetting, whereas the sky level *is* decreased by vignetting, and so the sky-subtracted density of saturated images will tend to increase towards the field edges.

The actual field response function is not necessarily radially symmetric due to differential emulsion desensitization (Dawe and Metcalfe 1982), but there are too few bright galaxies to measure the response as a function of 2-dimensional position on the plate. In order to estimate the response function, we have calculated the galaxy density in annular bins centred on each Schmidt field and then summed over all of the survey plates. By averaging over 180 fields, any real structure in the galaxy distribution on a scale $\sim$ plate size should be well averaged out. To compute the area of each annular bin that lies inside the scanned region of the plate, 5000 points were thrown down in the central $5^\circ \times 5^\circ$ square of each plate at random, avoiding drilled regions. The galaxy density, normalised by the density of random points is plotted in Figure 7. It can be seen that the normalised galaxy density lies within about one standard deviation of that for a random distribution as far as the field edges (2.5°), although there is marginal evidence for increasing galaxy density towards the field edges. Between the field edges and the extreme corners at $\sqrt{2} \times 2.5^\circ \approx 3.54^\circ$, the galaxy density drops to about 80% of that expected for a random distribution. For number counts in a Euclidean universe, $N(m) \propto 10^{0.6(m-m_0)}$, a twenty percent decrease in counts corresponds to a magnitude change $\delta m \approx 0.16$ mag. Only the extreme corners of the field suffer from serious vignetting, and these observed field effects are small enough not to significantly degrade the plate matching.

One might expect the observed field response function shown in Figure 7 to introduce a spurious signal in galaxy clustering estimated from the survey. A powerful technique for studying the effect of systematic errors on measured galaxy clustering is to compare the angular correlation function $w(\theta)$ calculated from pairs of galaxies on the same plate (intra-plate) and from pairs of galaxies on different plates (inter-plate). In Figure 8 we plot intra- and inter-plate estimates of $w(\theta)$ for APM-BGC galaxies. In this and other plots showing $w(\theta)$, the error bars are determined by dividing the survey area into four zones and calculating the variance in $w(\theta)$ measured using galaxies in each zone as 'centres' for the pair counts. These error estimates thus include the effects of clustering and cosmic variance, as well as Poisson statistics. We see that the intra- (solid symbols) and inter-plate (open symbols) estimates of $w(\theta)$ are in very good agreement, apart from some noise in the inter-plate estimate on small scales and a small excess in the last intra-plate estimate. This last point is less than 2σ away from the inter-plate estimate and carries negligible weight in the overall $w(\theta)$ from all galaxy pairs since the ratio of intra- to inter-plate pairs at this separation is 5×10^{-3}.

Another test which demonstrates that the field response function has a negligible effect on measured clustering is to generate the random points used in the $w(\theta)$ calculation with the *same* response function as the APM-BGC. In Figure 9 we plot $w(\theta)$ estimated using all (intra- plus inter-plate) galaxy pairs using both a uniform distribution of random points (solid symbols) and random points distributed with the same field response function as the galaxies (open symbols). We see no significant difference between the two estimates of $w(\theta)$, (indeed, in many cases the symbols are indistinguishable), thus confirming that the response function shown in Figure 7 has no deleterious effect on clustering measured from the APM-BGC.

3.2 Image Classification Consistency and Completeness

3.2.1 Consistency in Plate Overlaps

We have compared the assigned classifications of objects detected on more than one plate to test the consistency of image classification. A pair of image detections is included in this analysis if both image magnitudes are above the magnitude cut-off for their respective plates and if neither image is in a drilled region. Out of 14,358 galaxy images in the overlaps, where a galaxy is counted on *each* plate on which it was identified, 527 were checked on one plate but not on the other (*i.e.* the PRE was too 'stellar') and 252 objects were inspected on both plates, but classified as a galaxy on one plate, and non-galaxy on the other. Thus by using the PRE as a cutoff in deciding which images to eyeball, 3.7% of galaxies would not be checked in a single pass. An additional 1.8% were inspected but mis-classified half of the time. The actual incompleteness is likely to be higher than this since a very high surface-brightness galaxy might be classified as a star on both plates. Raster scans made of the bright images in twelve survey fields were used to investigate the overall completeness of the eyeball survey. The completenesses inferred range from 92.6% to 99.3% for the 12 fields, with a mean completeness of 96.3%, standard deviation 1.9%.

Table 2 shows frequencies of pair classifications in the overlaps. The classification codes are defined in Table 1, and type -1 denotes an image that was not checked (its PRE fell below the cutoff). Several features about the image classifications emerge from this table:

1. Over a third of noise images are also classified as stellar. This is because the diffraction spikes and haloes of many bright stars are detected as separate images, and it is often difficult to decide whether an image should be classified as a bright star or noise.
2. 42% of galaxies classified as elliptical are classified as lenticular on another occasion, and 24% of lenticulars are also classified as ellipticals. This illustrates the difficulty in distinguishing between the early-type galaxies, and the fact that there are more galaxies classified as lenticular than elliptical.
3. Nearly a quarter of lenticulars are also classified as spirals.
4. There is a large overlap between irregular galaxies and spirals.
5. Most galaxies in the unsure type category (type 5) are spirals, this is presumably because they are the most common.

External checks on the classification reliability and survey completeness are made by comparison with three other southern galaxy catalogues in § 4.

3.2.2 Consistency with Time

Given that the author had no experience of galaxy classification before starting this project, one might expect to see systematic variations in galaxy classification with time. Most of the fields were originally eyeballed in three batches; the second pass through was done in two batches. Table 3 shows the number of fields and galaxies eyeballed in each batch along with the percentage of galaxies of each morphological classification.

Clearly the ratio of elliptical to lenticular galaxies is much higher in batches 1 and 2 than in the later batches. The total number of early type galaxies (E plus S0) in batch 1 is slightly higher than the average. In batch 5 it is much lower than the others, and the fraction of spirals has risen accordingly. Nearly all of the galaxies classified as uncertain are in batch 2. For later batches, a greater effort was made to try and not use this class where possible. There are slightly more merged and multiple objects in batch 1 than the other batches.

To summarize, early type galaxies cannot be reliably distinguished between elliptical and lenticular. Batch 5 would appear to be deficient in early type galaxies.

If one combines elliptical and lenticular galaxies together, then the most discrepant batch regarding balance of morphological types is batch 5, which includes only 17.3% early-type galaxies compared with 74.9% late-types. In order to investigate what effect this might have on the estimated correlation function for different morphological types we have divided the survey into two regions: those plates included in batch 5 and all the rest. We then count galaxy pairs in which both galaxies lie in the same region (intra-region) and those pairs in different regions (inter-region). The intra- and inter-region estimates of $w(\theta)$ are shown in Figure 10. We see that given the noise in the inter-region estimate, the two estimates are in reasonable agreement for all types (a), although the intra-region estimate is biased slightly high relative to the inter-region estimate, an indication of small but systematic differences in galaxy density between the two regions. For early-type galaxies (b), we see a larger systematic difference between the intra- and inter-region estimates on scales 1–7 degrees, $\Delta w \approx 0.05$. The late-type estimates (c) are in reasonable agreement, although the inter-region estimate is very noisy on scales less than 2 degrees.

We thus conclude that systematic variations in galaxy classification reliability may introduce errors in the type-dependent $w(\theta)$ of order $\Delta w = 0.05$.

3.2.3 Consistency with Magnitude

To illustrate the dependence of classification on magnitude, in Figure 11 we show histograms of the fraction of each morphological type as a function of matched b_J magnitude. The number of ellipticals is roughly constant except for large fluctuations around $b_J \approx 14$ due to small number statistics. The number of lenticular galaxies is gradually increasing as the magnitude gets fainter. The combined early type number is dominated by the ellipticals at bright magnitudes and by the lenticulars at fainter magnitudes, where the overall trend is for increasing numbers of early type galaxies. Conversely, the number of spiral galaxies decreases at fainter magnitudes. This suggests

that as the images get fainter and spiral structure is harder to see, we are increasingly likely to classify a galaxy as a lenticular rather than a spiral if in doubt. Note that in the deeper ($b_J = 17.15$) Stromlo-APM Redshift Survey (Loveday *et al.* 1992) there is a bias *against* classifying the fainter galaxies as early-type, as they are instead classed as 'uncertain'. The fraction of galaxies classified as early type peaks near the magnitude limit of the APM-BGC. The fractions of irregular and 'uncertain' galaxies both increase at fainter magnitudes.

One should be aware of the magnitude-dependent bias in classification when interpreting type-dependent clustering results from the APM-BGC. See §7 for such an analysis.

4 Completeness and Classification Reliability: Comparison with other Catalogues

Two tests of the APM Bright Galaxy Catalogue are made in this section. Firstly we use the European Southern Observatory (ESO) Survey (Lauberts 1982) to identify any galaxies too large to be detected by the APM machine (see §2.3.1) and to check for galaxies found in the ESO survey which are missed or misclassified in the APM-BGC. We then compare our galaxy morphological classifications with three other southern galaxy catalogues.

4.1 Identification of Missing Galaxies

The ESO Survey, (Lauberts 1982), is a diameter limited galaxy catalogue, claimed to be complete to one arcminute, but also containing smaller disturbed galaxies, star clusters and planetary nebulae. The source material is the ESO(B) Atlas, taken in a blue waveband similar to the Johnson (B) colour, with the ESO 1m Schmidt in Chile. This survey covers the southern sky from -90 to -17.5 degrees in declination and so is ideal for comparison with the APM Bright Galaxy Catalogue.

Since the ESO catalogue is diameter limited to 1.0 arcmin, which corresponds to about 0.9 mm on a Schmidt plate, *all* galaxies too large to be detected by APM (§2.3.1) should be found in the ESO catalogue, assuming that the ESO and UKST plates reach a similar limiting isophote. There are an average of 32 ESO galaxies per Schmidt field, with an average of 29 per field lying within 60 arcseconds of a bright APM image. Those ESO galaxies outside APM holes which did not have an APM image identified as a galaxy within 1 arcmin were inspected by eye. Table 4 summarizes the outcome of the ESO-APM comparison; the final column of this Table indicates the percentage of ESO galaxies falling into each category. Those galaxies in category 3 were added to the list of eyeball identifications (with a flag set to show that they came from the ESO catalogue) and a separate list of large ESO galaxies (category 2) was compiled (Table 5). Thus about 3% of ESO galaxies were missed or misclassified (mostly the former) in the APM-BGC, and about 1.5% are too large to be detected by APM.

In order to check if any particular sort of galaxies were identified by ESO but missed in the APM-BGC, apart from the large (category 2) galaxies, *e.g.* high surface brightness compact ellipticals, we have looked at the distribution of morphological types and surface brightness for these galaxies. Table 6 shows the numbers and percentages of galaxies for each morphological type that were identified by ESO but not as galaxies in the APM-BGC ('missed', *i.e.* category 3 in Table 4) along

with galaxies identified in both the ESO and APM surveys ('found') for comparison. The relative percentages for the two groups are in reasonable agreement, except that the missed galaxies contain a larger fraction of class 8 objects (*i.e.* star-galaxy mergers) and a smaller fraction of elliptical galaxies, although the numbers of objects in both of these groups are rather small and subject to large random fluctuations.

The mean surface-brightness of an image, J_μ, measured in b_J mag arcsec^{-2}, is defined by

$$J_\mu = b_J + 2.5 \log A, \tag{3}$$

where b_J is the APM magnitude converted into the b_J system and A the area above the isophotal threshold in arcsec^2. In Figure 12 we plot the surface-brightness frequency histograms for (a) missed ESO galaxies, (b) found ESO galaxies and (c) all APM galaxies. In Figure 12(d) we plot the fraction of ESO galaxies that were missed as a function of surface brightness. It is clear that the missed ESO galaxies are biased towards high surface-brightness (HSB; $J_\mu \lesssim 22.5$) and in fact this plot provides a good estimate of our completeness as a function of surface brightness at the HSB end of the surface brightness range, assuming that the ESO survey is complete in this regime. Figure 12(e) shows the fraction of APM galaxies that were also identified in the ESO survey as a function of surface brightness. We see that those galaxies common to the two surveys tend to be of lower surface brightness than typical APM galaxies. It is not possible to use this comparison to quantify our incompleteness in LSB galaxies since (i) diameter-limited samples are expected to include LSB galaxies that would not be included even in a perfect magnitude-limited sample and (ii) any LSB galaxies that should have been seen in our sample may have not even been detected by the APM machine and inadvertently included in category 1 or 2 in Table 4.

4.2 Check on Galaxy Morphological Classification

As an external check on the reliability of morphological classifications of galaxies in the APM-BGC, we have compared morphological classifications of galaxies common to the APM-BGC and the ESO Surface Photometry Catalogue (Lauberts and Valentijn 1989), the Dressler (1980) cluster catalogue and the Corwin *et al.* (1985) Southern Galaxy Catalogue (SGC). Since the morphological types in these catalogues are coded into the de Vaucouleurs 'T-types' (de Vaucouleurs *et al.* 1976), (or a nearly equivalent system for Dressler's data), which sub-divide the coarser APM-BGC elliptical-lenticular-spiral classifications, they provide a good check on our classification reliability.

Tables 7, 8 and 9 compare morphological classifications in the SGC, Dressler and ESO catalogues respectively with APM-BGC classifications. The coding is generally in very good agreement except for the overlap between elliptical and lenticular galaxies, and to a lesser extent between lenticular and spiral galaxies. Of course, these catalogues are all shallower than the APM-BGC, and we expect slightly worse classification reliability at fainter magnitudes.

5 CCD Calibrations

The purpose of obtaining CCD calibrations was threefold: Firstly, to determine an overall zero-point for the APM magnitudes; secondly to check the plate matching procedure by testing for uniformity of the magnitudes over the survey area and thirdly to correct the magnitudes for the effects of photographic saturation.

5.1 Observations and Data Reduction

The photometric observations were carried out with the Siding Spring Observatory (SSO) 40-inch telescope CCD system in 1988 and 1990 and with the South African Astronomical Observatory (SAAO) 40-inch telescope CCD camera in 1988. Most of the galaxies observed were chosen from the Stromlo-APM Redshift Survey (Loveday *et al.* 1992), as well as a few sequences covering a wide magnitude range. For each galaxy, one 600s exposure was made in R and two 600s exposures in B_j (SSO) or B (SAAO). We also observed 21 E-region standard stars from the list of Couch and Newell (1980). Flat-field exposures of the twilight sky were made at the beginning and end of each night, weather permitting. Several bias frames were also recorded. Reduction of the CCD data followed the usual steps of bias-subtraction, fixing of bad columns and cosmic-rays, and flat-field division.

Images were detected and parameterized using the APM IMAGES software (Irwin 1985). This software provides the same set of parameters for CCD images as are determined by the APM machine from the photographic images, with the additional options of calculating total image intensities and deblending merged images. Both of these options were used. A detection threshold of 1.5 times *rms* sky noise was set. Any contiguous groups of 32 or more pixels (≈ 10 arcsec^2) above this threshold were analyzed. The two blue frames of each galaxy were co-added, after aligning the detected images, and IMAGES re-run on the co-added frame in order to minimize readout noise and lower the limiting isophote.

CCD magnitudes were corrected for atmospheric extinction using the extinction coefficients of Couch and Newell (1980) for the SSO data and of Walker (1984) for the SAAO data. The standard star observations were then used to transform the CCD magnitudes into the Couch and Newell (1980) B_J,R_F system using standard colour transform equations (*e.g.* Hardie 1962). The Couch and Newell system was chosen since their B_J band is designed to match the UK Schmidt J plate response function. Data was only used from those nights for which the standard star (observed − published) residuals were 0.05 mag or less.

5.2 CCD-APM Magnitude Comparisons

Determining galaxy magnitudes from the CCD frames and comparison with the APM magnitude needed to be done interactively due to the problems of merged images and occasional break-up of spiral-arm structure into sub-images.

The four sets of CCD images (one red, two blue and co-added blue) were displayed as ellipse maps and, working from a laser printer grey-scale plot, any broken images were indicated with the cursor. A new image intensity and position for the broken images was obtained by summing the intensities and calculating an intensity-weighted mean of positions of the bits. The images in the four frames were then matched up. The co-added blue frame was used to determine the CCD blue magnitude, and the difference between the single blue frames and co-added frame was used to estimate a blue magnitude error. Comparing the two blue frames is also a good test for photometric conditions since any cloud during the exposure would tend to make the blue magnitudes in one frame systematically higher or lower than the other. However, it is of course possible that cloud might affect only the red frame, which would alter the galaxy colours and hence the transform to standard magnitudes. We therefore rejected CCD frames if there was any doubt about the observing conditions being photometric. Airmass corrections were applied and the CCD magnitudes were transformed into

the Couch and Newell JF system using transform coefficients determined from the standard star observations. The CCD and APM images were paired up by displaying ellipse maps of both and indicating a few pairs with the cursor. These pairs were used to fit a 6-constant coordinate transform so that the remaining image pairs could be found automatically. Any broken APM images were summed together in the same way as broken CCD images. For each galaxy frame a file was written listing natural CCD J, R magnitudes; standard B_J, R_F magnitudes; APM zero-pointed magnitude and APM coordinates for each image in the frame. Bright galaxies were coded according to whether they were isolated images or merged with a star in the APM and/or CCD image analysis.

In Figure 13 we plot CCD B_J magnitude against matched, zero-pointed APM magnitude $m_{b_J} = 29.0 - m$. Merged and multiple galaxies have been excluded from this plot. The line is a quadratic least-squares fit to the CCD-APM magnitude relation assuming that the CCD magnitudes are error free. The transform from m_{b_J} to b_J is given by

$$b_J = -4.50 + 1.419 m_{b_J} - 0.00855 m_{b_J}^2. \tag{4}$$

After this saturation correction, the catalogue magnitude limit of $m_{b_J} = 16.37$ corresponds to $b_J = 16.44$. Brightward of $m_{b_J} = 16.37$, the scatter in CCD magnitude about the fit is 0.31 mag. This compares rather unfavourably with the *rms* error of 0.16 mag for the faint APM photometry (Maddox 1988, Maddox *et al.* 1990b), but is in reasonable agreement with the CCD-COSMOS photometric comparisons by Metcalfe *et al.* (1989) over a similar magnitude range. A sharp increase in CCD−COSMOS magnitude scatter brightward of $b_J \approx 17$ is very apparent from their Figure 1. The UK Schmidt J-plates provide reliable images down to $b_J \approx 21$ and for galaxy images brighter than $b_J \approx 16$, saturation is a serious problem.

Further details of the CCD photometry and the photometric data will be published separately.

5.3 Test of matching procedure

Figure 14 plots the CCD−APM magnitude residuals in an equal-area projection. In the absence of any large-scale gradients in the survey magnitude calibration, then these residuals should be uncorrelated with both themselves and with the plate zero points determined from overlap matching (§2.4), which are plotted in the same projection in Figure 6. To test for this we calculated the auto-correlation function of the CCD−APM residuals r_i, and the cross-correlation with the plate zero points z_i. The auto-correlation is plotted in Figure 15, where the error bars are given by $rms(r_i r_j)$ for each θ bin. The cross-correlation is plotted in Figure 16, where the error bars are given by $rms(r_i z_j)$. The CCD−APM residuals show marginal evidence for being anti-correlated on scales $\sim 15^\circ$, but only one separation bin shows this anti-correlation and it is less than a 3σ effect. The CCD−APM residuals are clearly uncorrelated with the plate zero-points, confirming the absence of any large-scale gradients in the survey photometry.

Since the *rms* scatter in individual APM magnitudes ≈ 0.31 mag and the *rms* magnitude error per overlap is only 0.05 mag, we would require CCD photometry for $N \gtrsim (0.31/0.05)^2 \approx 38$ galaxies per field to improve on the zero-points from overlap matching. Therefore the CCD magnitudes were not incorporated into the plate matching procedure.

6 The Catalogue

In compiling the 180 contiguous survey fields into one catalogue, the Cartesian plate coordinates were converted into right ascension and declination and only those galaxies within (RA, dec) boundaries equidistant from field centres were kept, thus avoiding duplication of galaxies in the overlaps. The magnitude limit for each field was set to $b_J = 16.44$ after applying the final field-corrections from overlap matching (§2.4) and correction for saturation (equation 4). Table 10 summarizes the galaxy numbers in the survey.

Figure 17 shows the galaxy distribution in an equal-area projection for all of the galaxies in the survey with $b_J \leq 16.44$. Figures 18–20 plot the early-type, late-type and merged galaxies respectively in the same projection. The stronger clustering of early-type galaxies over late-type is clearly visible, and an increase in star-galaxy mergers away from the SGP and towards the galactic plane is also apparent. The holes drilled around large images, step wedges and satellite trails are plotted in Figure 21

Table 11 presents the data in the APM Bright Galaxy Catalogue for a single survey field, number 076. The complete catalogue, along with the survey field centres and hole positions, is available from the Astronomical Data Centre (http://nssdc.gsfc.nasa.gov/adc/adc.html). Each column in the table is described below.

(1) Name: Each galaxy name is composed of the survey field number and the x, y position of the galaxy on the plate—this should ease location of any particular galaxy on the plate material. The first 3 digits are the SERC field number. The second set of digits are the x-position in millimetres from the centre of the plate (actually the APM scan centre). These are preceded by a '+' sign for galaxies to the right (west) of the plate centre or by a '−' sign for galaxies to the left (east) of centre. The final 3 digits are the y position, again in mm from the plate centre. A preceding '−' indicates galaxies above (north) of the plate centre, '+' indicates galaxies below (south) of the centre.

(2), (3) RA, dec: Right ascension (hours, minutes, seconds) and declination (degrees, arcminutes, arcseconds) in 1950 coordinates.

(4) b_J: Matched, saturation corrected b_J magnitude. Note that although two decimal places of precision are quoted, comparison with CCD photometry (§5.2) shows that individual galaxy magnitudes are accurate only to ≈ 0.3 mag.

(5), (6) maj, min: Major and minor diameter in arcseconds at threshold isophote.

(7) p.a.: Position angle in degrees measured clockwise from south-north line.

(8) Cl: Galaxy classification code, as given in Table 1. Those galaxies that were only found by cross-checking with the ESO survey (see §4.1) have had 10 added to the classification code.

7 Type-Dependent Clustering

In this section, we calculate the angular and spatial correlation function for all unmerged galaxies in the APM-BGC and for early and late type galaxies separately. A similar analysis was presented

by Loveday *et al.* (1995). We repeat the analysis here for a number of reasons. Firstly, use of an earlier, linear correction for photographic saturation from Loveday (1989) led to a corrected APM-BGC magnitude limit of $b_J = 16.57$ as opposed to $b_J = 16.44$ we obtain from equation (4). This affected the limber inversion carried out by Loveday *et al.* (1995). Secondly, in generating the random catalogue to correct for the survey boundaries, we inadvertently generated random points over five additional fields included in the Stromlo-APM survey, but not in the APM-BGC. This led to a scale-dependent overestimate of $w(\theta)$ by up to $\Delta w \approx 0.1$. Thirdly, in the current analysis we estimate errors by dividing the survey up into four zones and estimating $w(\theta)$ using galaxies in each zone in turn as centres. This is likely to give a more realistic estimate of the errors in $w(\theta)$ than the bootstrap resampling technique if the survey is affected by systematic variations in morphological classification, as suggested in §3.2.2.

Following Loveday *et al.* (1995), we have estimated $w(\theta)$ using the estimator

$$w(\theta) = \frac{N_{gg}(\theta)N_{rr}(\theta)}{[N_{gr}(\theta)]^2} - 1 + \Delta w, \tag{5}$$

where N_{gg}, N_{gr} and N_{rr} are the number of galaxy-galaxy, galaxy-random and random-random pairs at angular separation θ and Δw is a correction for the integral constraint,

$$\Delta w = \int\int_{\rm survey} w(\theta_{12}) d\Omega_1 d\Omega_2, \tag{6}$$

(Groth and Peebles 1977). The correction Δw is estimated in practice by calculating $w(\theta)$ without the correction, integrating $w(\theta)$ over all elements of solid angle $d\Omega_i$ in the survey area to obtain Δw and recalculating $w(\theta)$ with the correction added. A stable solution is rapidly reached by iteration.

Figure 22 shows $w(\theta)$ for all, early and late-type galaxies in the APM-BGC. We have fitted a power law $w(\theta) = A\theta^{1-\gamma}$ from 0.1 to 5° to these estimates, with results shown in Table 12. We see that early-type galaxies have a slightly steeper power law slope and a larger amplitude than late-type galaxies, in agreement with earlier determinations of the type-dependent angular correlation function (eg. Davis and Geller (1976) and Giovanelli *et al.* (1986)). The integral constraint corrections Δw shown in Table 12 make negligible difference to power-law fits on scales smaller than 5° but they do give some idea of possible systematic errors in the $w(\theta)$ estimates on large scales. The 'tail' in the early-type correlation function with $w \approx 0.01$ is almost certainly caused by variations in the classification consistency discussed in §3.2.2.

In order to estimate the spatial correlation functions $\xi(r)$, we have used these power law solutions in the relativistic version of Limber's equation (Groth and Peebles 1977, Phillipps *et al.* 1978) assuming $q_0 = 0.5$. The selection function $S(z)$ used in Limber's equation was determined separately for each galaxy type by smoothing the observed $N(z)$ for galaxies in the Stromlo-APM survey of the appropriate type and with $b_J < 16.44$ with a Gaussian of FWHM = 0.01. By using the measured selection function $S(z)$ directly in Limber's equation, we correct to first order for redshift-dependent biases in the morphological classification. The resulting parameters r_0 and B for the spatial correlation function $\xi(r) = (r/r_0)^{-\gamma} = Br^{-\gamma}$ are shown in Table 12. We confirm that at $r = 1h^{-1}$Mpc, the clustering amplitude of early-type galaxies is more than a factor of three higher than that of late-type galaxies.

8 Summary

We have described the construction of a catalogue of 14,681 galaxies brighter than $b_J = 16.44$ over a large fraction of the southern sky. The images were detected and parameterized by scanning 180 United Kingdom Schmidt Telescope plates with the Automated Plate Measuring system. Preliminary star-galaxy separation was carried out automatically using image profiles. All galaxy candidates were inspected by eye and assigned a morphological classification. A completeness of 97% was aimed for. By comparing image classifications in overlaps between plates (§3.2.1), we infer an actual completeness of 96.3%. As an external check on completeness, we correlated the ESO galaxy catalogue with the APM-BGC. We found that about 1.5% of ESO galaxies are too large to be detected by the APM machine (these galaxies are listed in Table 5) and a further 3% of ESO galaxies were detected by the APM machine but not classified as a galaxy in the APM-BGC. Overall, we estimate that the APM-BGC is at least 95% complete. Most of the incompleteness is due either to high surface brightness galaxies with star-like profiles (Fig. 12(d)) or low surface brightness galaxies which fall below our detection threshold. We plan to study surface-brightness selection effects in APM galaxy data in a future paper.

The reliability of the morphological classification in the APM-BGC was checked both internally using plate overlaps and externally by comparison with other catalogues. We conclude that the APM-BGC does not reliably distinguish between elliptical and lenticular galaxies; these classes should be combined in any statistical analysis. Time-dependent classification effects may produce an error in the type-dependent angular correlation function of $\Delta w \approx 0.05$. We classify fewer galaxies as late type at fainter magnitudes.

The photometry of the survey has been checked using CCD photometry of 259 galaxies. We fit a polynomial to the CCD versus APM magnitudes to correct for saturation and to define the magnitude zero-point. We find a scatter of 0.31 mag about this relation for individual galaxies. Comparison of the angular correlation functions calculated using intra- and inter-plate pairs of galaxies (§3.1) shows no evidence for significant plate-to-plate errors in photometry. The CCD−APM magnitude residuals are uncorrelated with each other and the plate zero-points, confirming the absence of large scale gradients in calibration.

The APM Bright Galaxy Catalogue is a reliable, new catalogue of bright galaxies which complements the fainter APM Galaxy Survey and the diameter-selected ESO survey. The catalogue is about 96% complete and has essentially zero contamination since every galaxy has been inspected by eye. It has proved to be a valuable source catalogue for the Stromlo-APM Redshift Survey (Loveday *et al.* 1992) and we hope that it will be useful for other followup work.

Acknowledgments

The major part of this work was carried out while the author was a graduate student at the University of Cambridge, and I thank the Institute of Astronomy and Jesus College, Cambridge, for their support. It is a great pleasure to thank the APM team (Mick Bridgeland, Pete Bunclark, Mike Irwin and Ed Kibblewhite) for making the APM galaxy surveys possible. Thanks also to Bruce Peterson who obtained some of the CCD photometry, to Somak Raychaudhury for helpful comments and to Bob Nichol for generating some finding charts. I am indebted to George Efstathiou and Steve Maddox for invaluable guidance, help and discussion throughout this project.

REFERENCES

Corwin, H.G., de Vaucouleurs, A. and de Vaucouleurs, G., 1985, Univ of Texas Monographs in Astronomy, No. 4

Couch, W.J. and Newell, E.B., 1980, PASP, 92, 746

Davis, M. and Geller, M.J., 1976, ApJ, 208, 13

Davis, M., Efstathiou, G., Frenk, C.S. and White, S.D.M., 1985, ApJ, 292, 371

Dawe, J.A. and Metcalfe, N., 1982, Proc. ASA, 4, 466

de Vaucouleurs, G., de Vaucouleurs, A. and Corwin, H.G., 1976, Second Reference Catalogue of Bright Galaxies, Univ. Texas Press, Austin

Dressler, A., 1980, ApJS, 42, 565

Giovanelli, R., Haynes, M.P. and Chincarini, G.L., 1986, ApJ, 300, 77

Groth, E.J. and Peebles, P.J.E., 1977, ApJ, 217, 385

Hardie, R.H., 1962, in Astronomical Techniques, ed. W.A. Hiltner, (Univ. Chicago Press), p178

Irwin, M.J., 1985, MNRAS, 214, 575

Kibblewhite, E.J., Bridgeland, M.T., Bunclark, P. and Irwin, M.J., 1984, in Astronomical Microdensitometry Conference, NASA Conf. Pub. 2317, p277

Lauberts, A., 1982, The ESO/Uppsala Survey of the ESO(B) Atlas, European Southern Observatory

Lauberts, A. and Valentijn, E.A., 1989, The Surface Photometry Catalogue of the ESO-Uppsala Galaxies, European Southern Observatory

Loveday, J., 1989, Ph.D. Thesis, University of Cambridge

Loveday, J., Peterson, B.A., Efstathiou, G. and Maddox, S.J., 1992, ApJ, 390, 338

Loveday, J., Maddox, S.J., Efstathiou, G., and Peterson, B.A., 1995, ApJ, 442, 457

Maddox, S.J., 1988, Ph.D. Thesis, University of Cambridge

Maddox, S.J., Sutherland, W.J. Efstathiou, G., and Loveday, J., 1990a, MNRAS, 243, 692

Maddox, S.J., Efstathiou, G. and Sutherland, W.J., 1990b, MNRAS, 246, 433

Maddox, S.J., Sutherland, W.J. Efstathiou, G., Loveday, J. and Peterson, B.A., 1990c, MNRAS, 247, 1P

Maddox, S.J., Efstathiou, G., Sutherland, W.J. and Loveday, J., 1990d, MNRAS, 242, 43P

Metcalfe, N., Fong, R., Shanks, T. and Kilkenny, D., 1989, MNRAS, 236, 207

Phillipps, S., Fong, R., Ellis, R.S., Fall, S.M. and MacGillivray, H.T., 1978, MNRAS, 182, 673

Raychaudhury, S., 1989, Nature, 342, 251

Raychaudhury, S., Lynden-Bell, D., Scharf, C., and Hudson, M.J., 1994, Abstracts, 184th AAS Meeting, Minnesota

Shane, C.D. and Wirtanen, C.A., 1967, Pub. Lick. Obs., 22, Part 1

UKSTU handbook, 1983, Royal Observatory, Edinburgh

Walker, A.R., 1984, CCD Photometry using ASPIC Programs, SAAO publication

Zwicky, F., Herzog, E., Wild, P., Karpowicz, M. and Kowal, C., 1961–68, Catalog of Galaxies and Clusters of Galaxies, Vols. I–VI, California Institute of Technology, Pasadena

Tables

Table 1: Image classification coding scheme

Code	Description
−1	Image not checked
0	Noise (*e.g.* dust, satellite trail, diffraction spike)
1	Elliptical galaxy
2	Lenticular galaxy
3	Spiral galaxy
4	Irregular/peculiar galaxy or very low surface-brightness
5	Galaxy, type unsure
6	Star
7	Multiple stellar
8	Merged stellar/galaxy image
9	Multiple galaxy

Table 2: Comparison of image classifications for objects detected more than once. The classification codes are defined in Table 1.

	Classification Code										
	−1	0	1	2	3	4	5	6	7	8	9
−1	—										
0	217	128									
1	53	7	314								
2	47	10	425	802							
3	275	80	147	426	3292						
4	14	6	6	14	248	112					
5	16	0	23	16	85	6	12				
6	14376	303	5	4	13	1	0	4335			
7	1507	50	0	2	5	1	0	611	1888		
8	83	8	13	29	44	14	0	67	42	256	
9	11	5	12	21	23	16	1	0	2	17	79
Total	16599	814	1005	1796	4638	438	159	19715	4108	573	187

Table 3: The number of fields and galaxies eyeballed in each batch, with the percentage of each morphological classification.

			Galaxy Classification Code						
Batch	Fields	Galaxies	1	2	3	4	5	8	9
1: 24 Mar 87–02 Apr 87	18	2730	35.8	3.7	47.0	1.7	0.4	8.3	3.0
2: 29 Apr 87–04 Jun 87	25	3603	26.3	5.6	49.5	3.1	9.2	4.7	1.7
3: 12 Jul 87–18 Aug 87	130	17341	5.6	24.7	55.8	4.9	0.4	6.9	1.8
4: 12 Sep 87–30 Sep 87	24	1733	0.1	34.4	53.2	4.3	0.0	6.8	1.2
5: 20 Jun 88–22 Jul 88	67	6926	0.3	17.0	71.3	3.6	0.0	5.4	2.5

Table 4: Results from ESO-APM comparison

Category	Description	%
1	Estimated to be fainter than the APM-BGC magnitude limit.	10.7
2	Too large to be detected by APM.	1.5
3	Matched up with an APM image not classified as a galaxy.	3.0
4	Matched up with an APM galaxy.	78.7
5	No match found; either due to a discrepancy in the coordinate systems or a 'noise' ESO object.	6.1

Table 5: Large ESO galaxies missing from the APM Bright Galaxy Catalogue. RA, dec are in J2000.0 coordinates.

	RA			Dec		ESO Name
1	12	13.5	-58	14	48.1	113- G 023
2	32	34.6	-60	12	43.9	115-IG 018
3	13	3.8	-57	21	26.1	116- G 012
22	8	33.6	-57	26	34.7	146- G 009
23	58	59.8	-55	27	23.4	149- G 007
0	1	5.8	-53	59	29.8	149- GA011
1	47	43.1	-52	45	40.1	152- G 024
3	35	57.8	-52	39	1.7	156- G 001
4	4	3.0	-54	6	10.1	156- G 036
4	9	51.3	-56	7	15.1	157- G 003
4	15	45.0	-55	35	31.7	157- G 016
4	20	0.4	-54	56	18.6	157- G 020
4	21	27.8	-55	56	0.3	157- G 021
4	21	59.1	-56	58	26.7	157- G 022
4	27	37.8	-55	1	36.5	157- G 031
21	36	28.6	-54	33	26.2	188- G 012
23	33	16.1	-54	5	38.3	192- G 007
3	57	42.8	-48	54	27.7	201- G 012
21	19	0.3	-48	33	49.8	236- G 001
21	46	10.2	-52	15	55.9	188-IG 019
21	52	42.8	-48	15	15.7	237- G 011
22	2	41.3	-51	17	47.5	237- G 027
0	39	1.3	-43	4	30.8	242-IG 022
3	38	44.9	-44	5	59.1	249- G 011
3	44	31.9	-44	38	38.3	249- G 016
21	15	8.0	-47	13	13.2	286- G 079
21	32	35.1	-44	4	0.1	287- G 036
23	14	49.1	-43	35	28.7	291- G 010
23	18	23.2	-42	21	41.5	291- G 016
23	33	14.7	-45	0	57.4	291- G 029
23	33	17.7	-45	0	21.4	291- G 028
2	33	34.1	-39	2	45.7	299- G 007
3	17	17.5	-41	6	28.3	301- G 002
3	51	40.8	-38	27	4.0	302- G 014
5	7	42.7	-37	30	44.8	305- G 008
22	33	52.5	-40	55	59.8	345- G 026
22	55	0.7	-39	39	41.5	346- G 012
23	2	10.0	-39	34	8.7	346- G 026
23	36	14.5	-37	56	23.3	347- G 028
23	57	55.1	-32	35	47.1	349- G 012

Table 5, continued

RA			Dec			ESO Name
1	22	43.4	-36	34	44.7	352- G 060
3	30	34.8	-34	51	12.3	358- G 012
3	33	35.6	-36	8	23.0	358- G 017
3	35	16.7	-35	13	34.6	358- G 023
3	36	27.9	-34	58	32.7	358- G 028
3	37	11.7	-35	44	41.7	358- G 038
3	38	29.0	-35	26	57.9	358- G 045
3	38	51.7	-35	35	35.6	358- G 046
3	42	19.6	-35	23	36.0	358- G 052
3	47	5.5	-33	42	40.9	358- G 065
4	12	4.3	-32	52	21.0	359- G 027
22	8	28.3	-34	6	23.2	404- G 032
23	22	4.4	-33	22	31.9	407- G 016
0	52	41.7	-31	12	18.6	411- G 025
2	46	18.9	-30	16	21.4	416- G 020
3	18	15.1	-27	36	35.5	418- G 001
3	28	19.0	-31	4	4.4	418- G 005
3	39	22.6	-31	19	19.9	418- G 015
4	13	40.9	-31	38	46.2	420- G 012
22	5	48.7	-28	59	22.4	467- G 001
22	14	39.6	-27	39	46.4	467- G 028
22	27	22.9	-31	0	29.1	467- G 063
22	42	17.9	-30	3	28.9	468- G 023
23	12	7.6	-28	32	28.6	469- G 019
23	27	2.2	-31	56	53.3	470- G 007
0	9	53.4	-24	57	11.5	472- G 016
0	13	58.7	-23	11	2.8	473- G 001
0	47	34.4	-25	17	32.0	474- G 029
2	25	3.6	-24	48	51.3	478- G 028
2	26	21.8	-24	17	32.1	479- G 004
3	2	37.6	-22	52	3.8	480- G 023
3	19	50.8	-26	3	36.9	481- G 020
3	39	1.8	-22	34	20.0	482- G 024
4	21	35.6	-27	7	40.9	484- G 010
2	23	4.7	-21	13	58.0	545- G 011
3	5	58.7	-19	23	32.5	547- G 009
3	12	57.6	-17	55	42.4	547- G 020
3	24	38.4	-19	18	22.3	548- G 009
3	32	2.6	-20	49	20.5	548- G 031
3	44	50.4	-21	55	20.6	549- G 009
3	45	22.0	-18	38	4.5	549- G 012

Table 5, continued

RA			Dec			ESO Name
3	48	14.7	-21	28	27.2	549- G 018
4	6	49.9	-21	10	43.1	550- G 007
4	42	14.3	-20	26	4.1	551- G 027
22	8	19.4	-19	3	55.8	601- G 021
22	44	26.8	-20	2	7.3	603- G 008
22	50	58.0	-21	59	52.9	603- G 019

Table 6: Numbers and frequencies of galaxy types missed and found in comparison with the ESO catalogue. The classification codes are those defined in Table 1.

Class	Missed		Found	
	No.	%	No.	%
1	6	3.09	441	9.06
2	20	10.31	434	8.91
3	136	70.10	3404	69.90
4	8	4.12	320	6.57
5	0	0.00	34	0.70
8	14	7.22	89	1.83
9	10	5.15	148	3.04
Total	194	100.00	4870	100.00

Table 7: Corwin *et al.* T-type *versus* APM eyeball classification frequencies.

Corwin		APM Eyeball Classification							
T-type	Hubble	1	2	3	4	5	8	9	Total
−6	cE	1	0	0	1	0	0	0	2
−5	E0	34	12	1	2	0	1	3	53
−4	E+	33	19	0	0	0	2	5	59
−3	S0-	95	39	4	0	0	1	1	140
−2	S0	60	74	52	5	1	0	3	195
−1	S0+	17	21	40	1	2	0	0	81
0	S0/a	2	9	51	2	1	1	0	66
1	Sa	0	5	96	5	0	0	0	106
2	Sab	1	2	78	0	0	0	0	81
3	Sb	3	3	180	0	0	0	1	187
4	Sbc	1	0	154	0	0	0	1	156
5	Sc	0	0	193	0	0	3	0	196
6	Scd	0	0	80	2	0	0	0	82
7	Sd	0	1	55	11	0	0	0	67
8	Sdm	0	0	41	8	0	0	0	49
9	Sm	0	1	34	27	0	2	0	64
10	Im	0	0	19	30	0	2	1	52
	Total	247	186	1078	94	4	12	15	1636

Table 8: Dressler T-type *versus* APM eyeball classification frequencies.

Dressler		APM Eyeball Classification							
T-type	Hubble	1	2	3	4	5	8	9	Total
−5	E0	8	14	0	0	0	0	1	23
−4	E+	2	1	0	0	0	0	0	3
−3	S0-	2	4	0	0	0	0	1	7
−2	S0	7	19	15	0	0	3	1	45
0	S0/a	0	6	5	0	0	1	0	12
1	Sa	1	9	13	0	0	0	1	24
2	Sab	0	0	4	0	0	0	1	5
3	Sb	2	2	28	0	0	2	0	34
4	Sbc	0	0	3	0	1	1	0	5
5	Sc	1	2	12	0	2	0	0	17
6	Scd	0	2	6	2	0	1	0	11
8	Sdm	0	0	1	0	0	0	0	1
10	Im	0	0	1	1	0	1	0	3
11	cI	2	4	7	0	0	3	0	16
	Total	25	63	95	3	3	12	5	206

Table 9: ESO T-type *versus* APM eyeball classification frequencies.

ESO		APM Eyeball Classification							
T-type	Hubble	1	2	3	4	5	8	9	Total
−5	E0	52	20	8	2	1	0	5	88
−4	E+	42	20	1	0	0	3	4	70
−3	S0-	123	74	23	0	0	3	2	225
−2	S0	85	121	121	9	6	8	8	358
−1	S0+	39	50	85	4	0	4	1	183
0	S0/a	21	41	158	11	3	2	4	240
1	Sa	21	40	461	22	8	5	11	568
2	Sab	13	27	210	10	2	9	19	290
3	Sb	6	9	692	24	3	2	26	762
4	Sbc	4	4	304	11	0	3	10	336
5	Sc	1	5	287	15	0	9	10	327
6	Scd	2	1	476	15	3	13	13	523
7	Sd	1	5	155	45	6	6	12	230
8	Sdm	2	0	122	34	0	2	6	166
9	Sm	1	1	59	47	0	5	4	117
10	Im	1	2	56	62	1	5	1	128
	Total	414	420	3218	311	33	79	136	4611

Table 10: Summary of galaxy counts in the complete catalogue ($b_J \leq 16.44$).

Galaxy Type	Number	%
Elliptical	1791	12.2
lenticular	2648	18.0
Spiral	8217	56.0
Irregular/Peculiar	627	4.3
Unsure	164	1.1
Merged with star	975	6.6
Multiple	259	1.8
Total	14681	100.0
Holes drilled	1456	—

Table 11: The APM Bright Galaxy Catalogue for field 076

Name	RA			Dec			b_J	maj	min	p.a.	Cl
076-086-127	22	48	53.59	-67	41	10.0	15.65	41	28	150	3
076-069-060	22	46	18.04	-68	57	21.3	14.67	69	30	156	3
076-060-049	22	44	39.38	-69	10	1.4	14.28	64	45	177	3
076-055-049	22	43	38.60	-69	10	14.4	16.14	48	20	115	2
076-039-099	22	39	49.52	-68	15	8.3	15.88	35	18	55	3
076-033-110	22	38	41.63	-68	2	49.9	15.59	43	29	61	2
076-015-079	22	35	0.24	-68	38	8.3	16.36	35	24	169	2
076-009-052	22	34	1.52	-69	7	57.7	15.68	36	24	175	13
076+022-124	22	27	41.23	-67	47	50.9	16.17	31	21	11	3
076+058-111	22	20	30.09	-68	0	35.6	16.41	33	21	8	2
076+065-133	22	19	12.69	-67	35	25.1	16.44	24	17	5	3
076+069-114	22	18	17.69	-67	56	23.4	16.10	34	23	10	3
076+100-103	22	12	6.23	-68	6	33.0	16.18	51	30	124	4
076+105-125	22	11	27.23	-67	41	33.8	15.52	43	31	108	3
076+106-066	22	10	13.79	-68	46	43.0	15.97	51	25	99	3
076+112-059	22	8	42.68	-68	54	31.7	14.56	62	43	72	2
076+117-126	22	9	4.61	-67	39	45.6	15.64	39	33	171	2
076+121-120	22	8	14.48	-67	45	21.6	16.26	46	14	156	3
076-116+007	22	57	29.69	-70	7	17.7	16.11	31	22	150	8
076-113-015	22	56	20.68	-69	43	6.7	16.42	41	17	52	3
076-108-037	22	54	51.23	-69	19	14.2	14.15	91	39	31	3
076-099-007	22	53	32.00	-69	53	20.9	15.89	43	24	80	3
076-090+043	22	52	28.98	-70	50	27.6	14.82	48	46	132	2
076-087+046	22	51	56.43	-70	53	53.9	15.26	75	26	174	3
076-078-031	22	48	34.08	-69	29	8.8	15.68	34	27	155	3
076-060-032	22	44	43.85	-69	28	37.5	15.40	59	29	165	3
076-058+021	22	44	58.11	-70	27	38.5	15.57	70	19	11	3
076-055-040	22	43	39.90	-69	20	13.8	16.15	56	14	124	3
076-044-006	22	41	31.72	-69	58	52.4	16.07	32	28	81	3
076-026+041	22	37	56.04	-70	52	18.7	16.11	31	23	18	9
076-024-008	22	37	10.65	-69	57	20.6	15.75	46	21	40	8
076+001+023	22	31	43.20	-70	32	25.9	14.69	60	45	41	3
076+003-009	22	31	25.89	-69	56	0.7	16.26	28	28	90	2
076+006-014	22	30	42.23	-69	50	58.5	16.17	41	17	107	8
076+020+043	22	27	32.88	-70	54	33.2	16.22	84	9	31	3
076+037+029	22	23	41.67	-70	38	37.1	15.03	48	39	65	3
076+038-044	22	24	5.04	-69	16	45.3	16.42	33	24	45	2
076+039+036	22	23	15.83	-70	46	13.9	16.35	65	9	86	3
076+044+039	22	22	3.71	-70	49	19.9	16.39	33	20	161	3
076+047-006	22	21	54.39	-69	58	21.2	16.28	33	27	107	3
076+056+021	22	19	29.76	-70	27	48.5	16.43	29	14	14	3

Table 11, continued

Name	RA			Dec			b_J	maj	min	p.a.	Cl
076+058+029	22	19	0.17	-70	37	7.8	15.76	36	34	115	2
076+070+034	22	16	14.59	-70	42	0.2	16.06	38	24	69	3
076+097+053	22	9	46.39	-71	0	52.9	16.28	26	25	117	3
076+099+045	22	9	34.21	-70	51	7.6	15.37	43	26	80	8
076+099-022	22	10	48.25	-69	36	55.1	15.04	104	17	106	3
076+100+022	22	9	39.87	-70	25	37.6	16.41	36	19	169	4
076+111+021	22	7	21.16	-70	23	54.8	15.58	63	14	21	3
076+110+033	22	7	16.35	-70	37	2.2	16.21	42	14	102	8
076-099+103	22	55	56.05	-71	56	36.4	16.12	32	17	148	3
076-058+109	22	46	4.85	-72	5	52.3	16.11	49	15	84	3
076-053+090	22	44	36.86	-71	45	56.8	16.42	37	21	77	2
076-050+077	22	43	54.56	-71	31	10.3	16.12	68	10	9	3
076-049+120	22	44	0.94	-72	18	59.0	16.06	33	32	57	3
076-046+073	22	42	46.51	-71	27	2.5	16.01	45	32	70	3
076-044+080	22	42	29.15	-71	35	10.7	15.32	45	35	50	2
076-030+087	22	39	17.03	-71	43	23.9	15.86	34	27	33	3
076-020+075	22	36	42.77	-71	30	8.5	15.28	50	26	62	3
076-017+057	22	35	54.92	-71	10	20.8	16.29	46	17	86	3
076+021+079	22	27	4.40	-71	34	35.9	16.34	54	12	103	3
076+024+086	22	26	28.53	-71	42	4.2	15.89	35	32	172	1
076+027+083	22	25	38.44	-71	38	35.9	16.41	30	26	86	2
076+030+066	22	24	59.38	-71	19	47.6	16.27	32	30	88	3
076+033+060	22	24	31.23	-71	12	33.6	16.34	31	19	170	4
076+038+095	22	22	54.57	-71	52	7.0	15.85	59	16	91	3
076+060+089	22	17	45.33	-71	43	57.2	16.43	34	20	23	3
076+060+074	22	17	57.49	-71	27	30.9	14.93	76	25	165	8
076+082+120	22	12	4.38	-72	16	27.0	16.06	63	11	105	3
076+083+092	22	12	13.65	-71	45	15.4	14.81	54	39	166	3
076+092+096	22	10	8.55	-71	49	27.6	15.79	60	16	172	3
076+095+106	22	9	3.54	-71	59	38.4	15.57	44	35	122	4
076+100+072	22	8	43.43	-71	21	3.7	15.22	59	21	117	3
076+106+104	22	6	35.49	-71	57	3.6	15.96	59	15	179	3
076+108+086	22	6	23.34	-71	35	58.7	15.64	58	29	55	3

Table 12: Angular correlation function results for all, early and late type galaxies in the APM-BGC.

Type	γ	A	Δw	B	r_0
All	1.85 ± 0.14	0.18 ± 0.03	2.9×10^{-3}	16.4 ± 1.5	4.5 ± 0.6
Early	1.93 ± 0.16	0.35 ± 0.05	4.6×10^{-3}	40.6 ± 3.5	6.8 ± 0.8
Late	1.79 ± 0.16	0.15 ± 0.03	1.6×10^{-3}	11.3 ± 1.0	3.9 ± 0.5

Note.—Power-law fits ($w = A\theta^{1-\gamma}$) were made over the range 0.1–5°. The integral constraint Δw is estimated from the observed $w(\theta)$. The amplitude, B, and corresponding scale length, r_0 are for the spatial correlation function inferred from inverting Limber's equation.

Figure Captions

Figure 1 An equal-area projection of the fields included in the APM Bright Galaxy Catalogue. The UKSTU field numbers are indicated, along with lines of constant RA and dec.

Figure 2 Areal profiles for (a) stars and (b) galaxies in the APM magnitude range 12.5–12.6 on one survey plate.

Figure 3 Profile residual error ε plotted against APM magnitude for one survey field. Dots denote stars, plus signs galaxies, asterisks multiple-stars, six-pointed stars star-galaxy mergers and open crosses multiple galaxies. Open squares show 'noise' images.

Figure 4 Overlap magnitude errors (a) before and (b) after plate matching.

Figure 5 Histogram of plate zero-point corrections from matching procedure.

Figure 6 Plate corrections after final matching, plotted in the same equal area projection as Figure 1. The line to the bottom-left shows a magnitude correction of 0.5 mag.

Figure 7 Galaxy density as a function of distance from the field centre, obtained by stacking all of the survey plates and normalizing by a random distribution of points within the field boundaries and outside drilled regions.

Figure 8 The angular correlation function $w(\theta)$ for APM-BGC galaxies from intra-plate pairs (solid symbols) and inter-plate pairs (open symbols). Error bars are determined from the variance between four zones.

Figure 9 The angular correlation function $w(\theta)$ from all pairs of APM-BGC galaxies measured using a uniform random catalogue (solid symbols) and a random catalogue with the field response function shown in Figure 7 (open symbols).

Figure 10 The angular correlation function $w(\theta)$ from intra-region pairs (solid symbols) and inter-region pairs (open symbols) for (a) all galaxy types, (b) early type galaxies and (c) late type galaxies. The two regions consist of (i) plates eyeballed in batch 5 (Table 3) and (ii) all the rest.

Figure 11 Histograms of fraction of each morphological type as a function of matched b_J magnitude.

Figure 12 Surface-brightness frequency histograms for (a) missed ESO galaxies, (b) found ESO galaxies, (c) all APM galaxies, (d) fraction of galaxies missed and (e) fraction of APM galaxies also detected by ESO survey.

Figure 13 Total CCD B_J magnitudes plotted against APM magnitudes for 259 unmerged galaxies. The line shows the quadratic fit that we have used to convert photographic magnitudes to the B_J system. The scatter about this line brightward of $m_{b_J} = 16.37$ (shown by the vertical dotted line) is 0.31 mag.

Figure 14 CCD−APM magnitude residuals plotted in the same equal area projection as Figure 1. The line in the bottom-left corner shows a magnitude residual of 0.5 mag.

Figure 15 Auto-correlation function of the CCD−APM magnitude residuals.

Figure 16 Cross-correlation of plate zero points with CCD−APM residuals.

Figure 17 All 14,681 galaxies in the APM bright galaxy survey plotted in the same equal area projection as Figure 1.

Figure 18 The 4439 early-type (elliptical plus lenticular) galaxies.

Figure 19 The 8844 late-type (spiral plus irregular) galaxies.

Figure 20 The 975 star-galaxy and galaxy-galaxy merged images.

Figure 21 The 1456 holes drilled in the survey.

Figure 22 The angular correlation functions $w(\theta)$ for all (open circles), early-type (filled circles) and late-type (filled squares) galaxies in the APM Bright Galaxy Catalogue. The dotted lines show power-law fits from 0.1 to 5°.

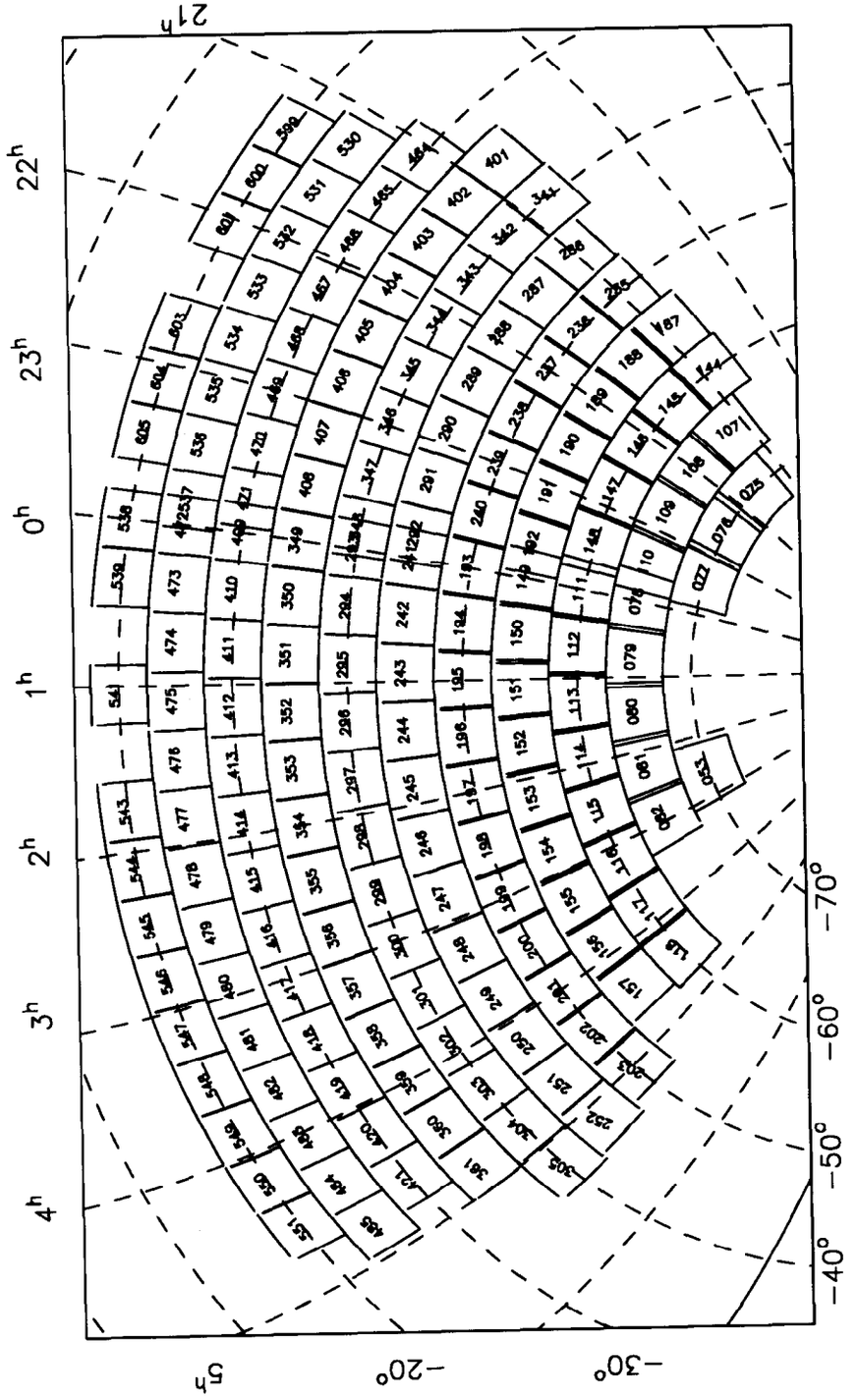

Figure 1:

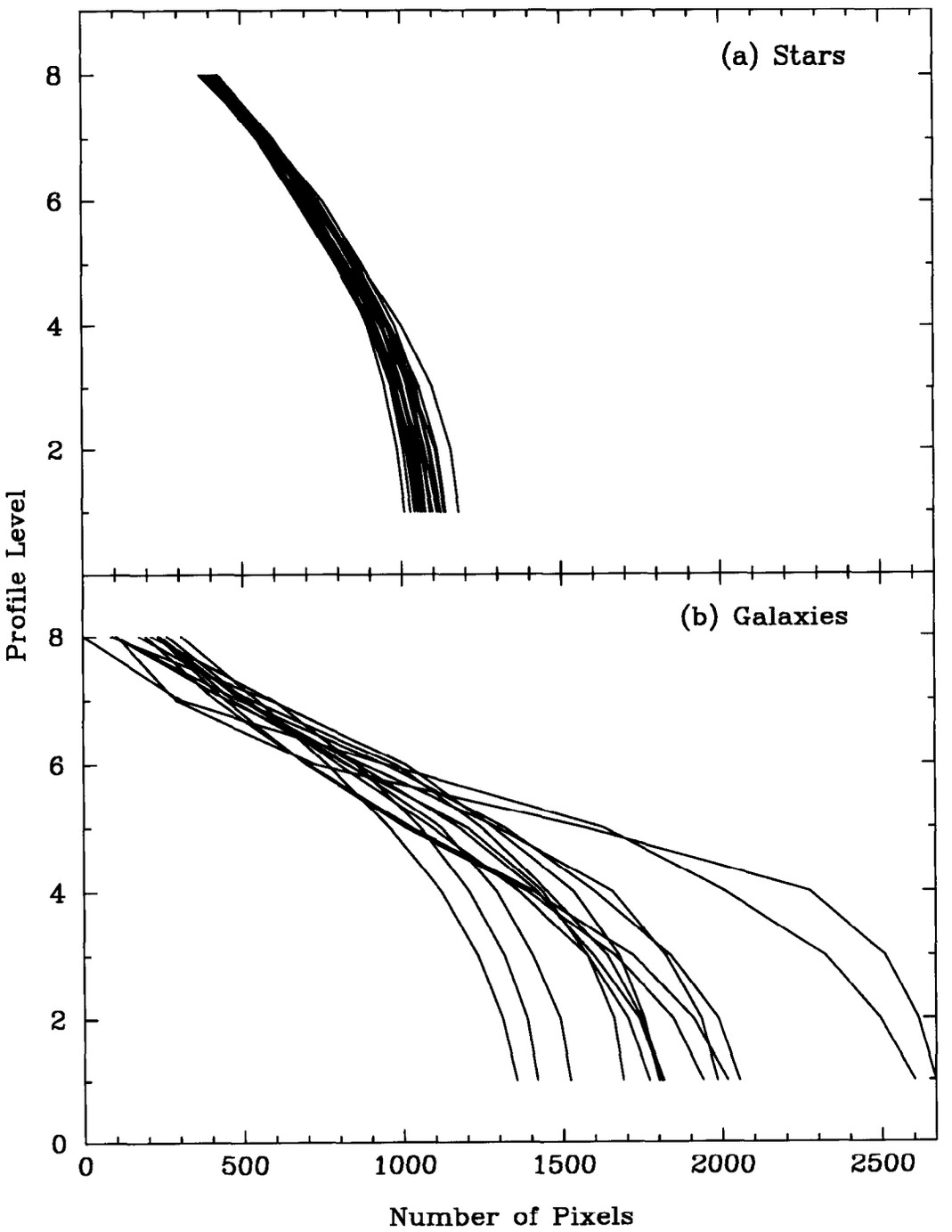
(a) Stars
(b) Galaxies
Profile Level
Number of Pixels
0
2
4
6
8
0
500
1000
1500
2000
2500

Figure 2:

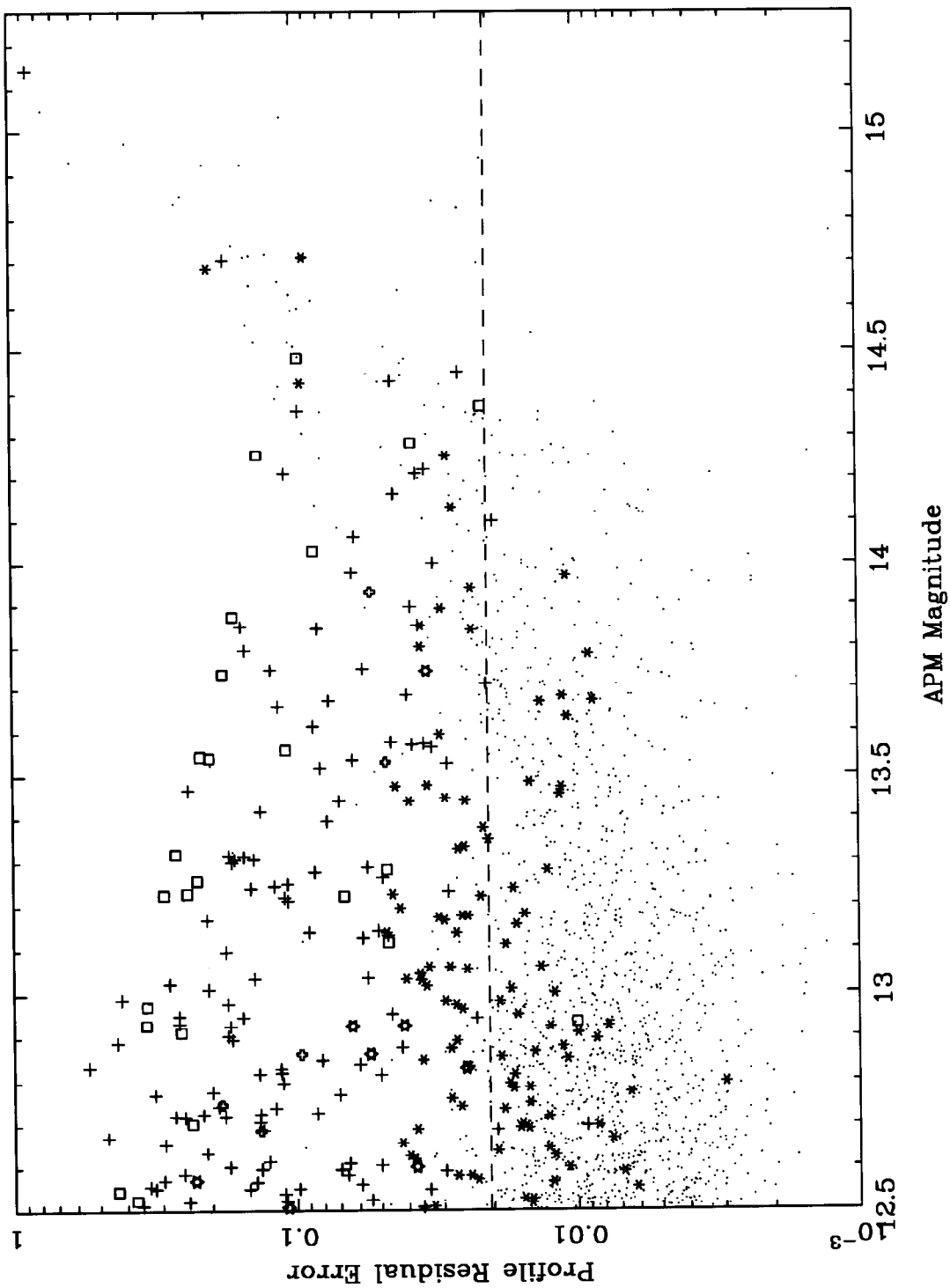
Profile Residual Error
1
0.1
0.01
10^{-3}
APM Magnitude
12.5
13
13.5
14
14.5
15

Figure 3:

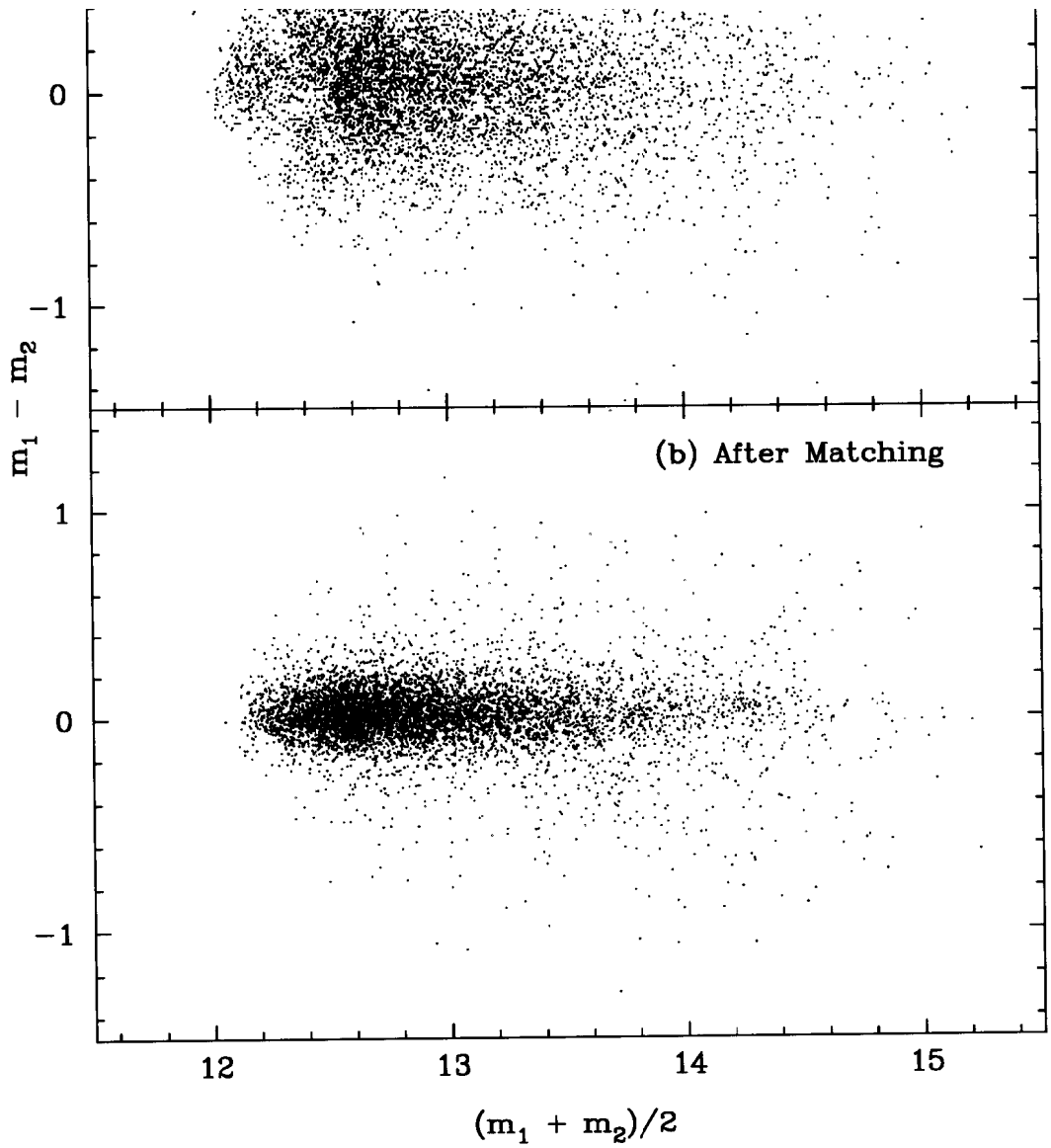

Figure 4:

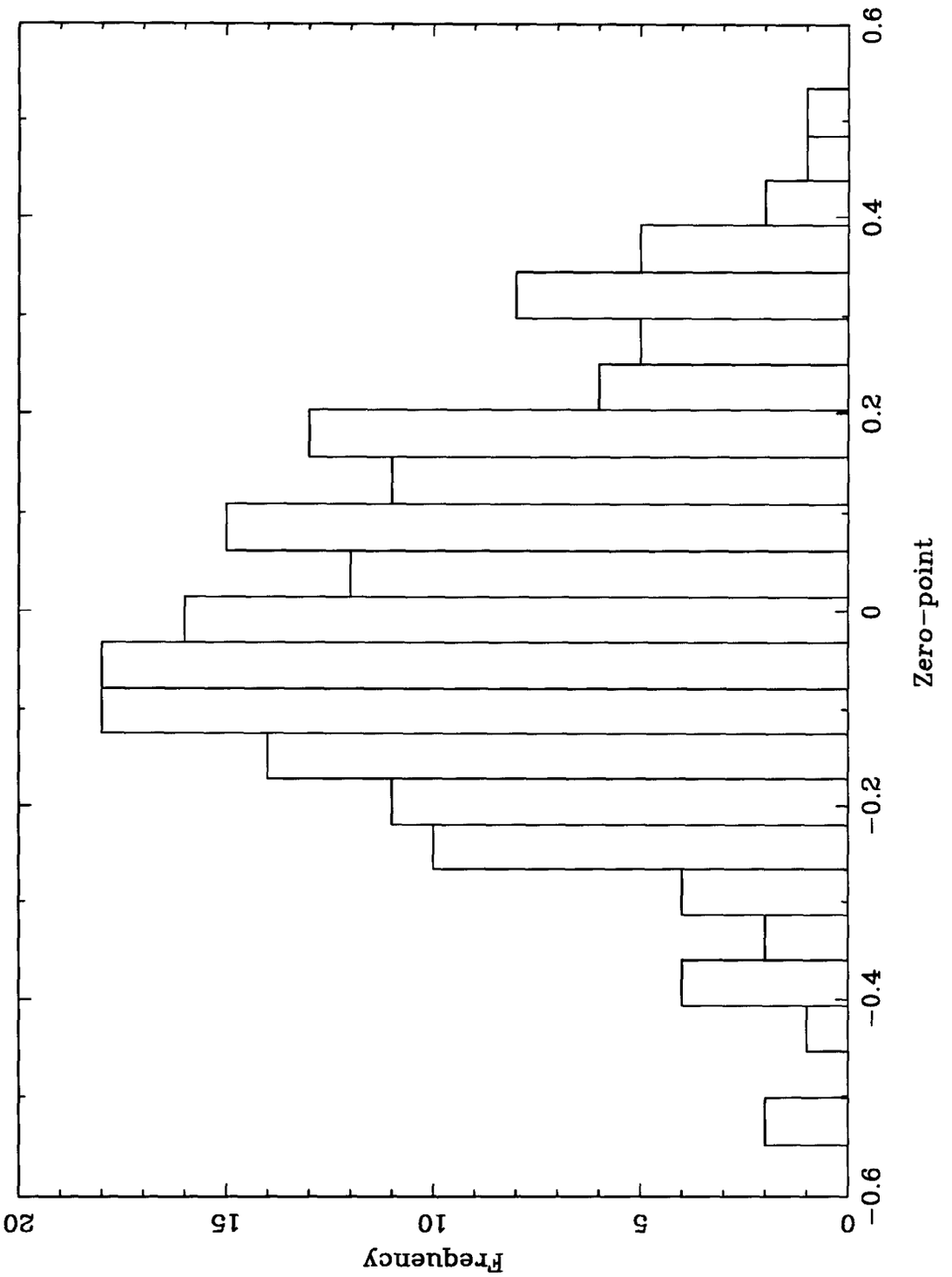

Figure 5:

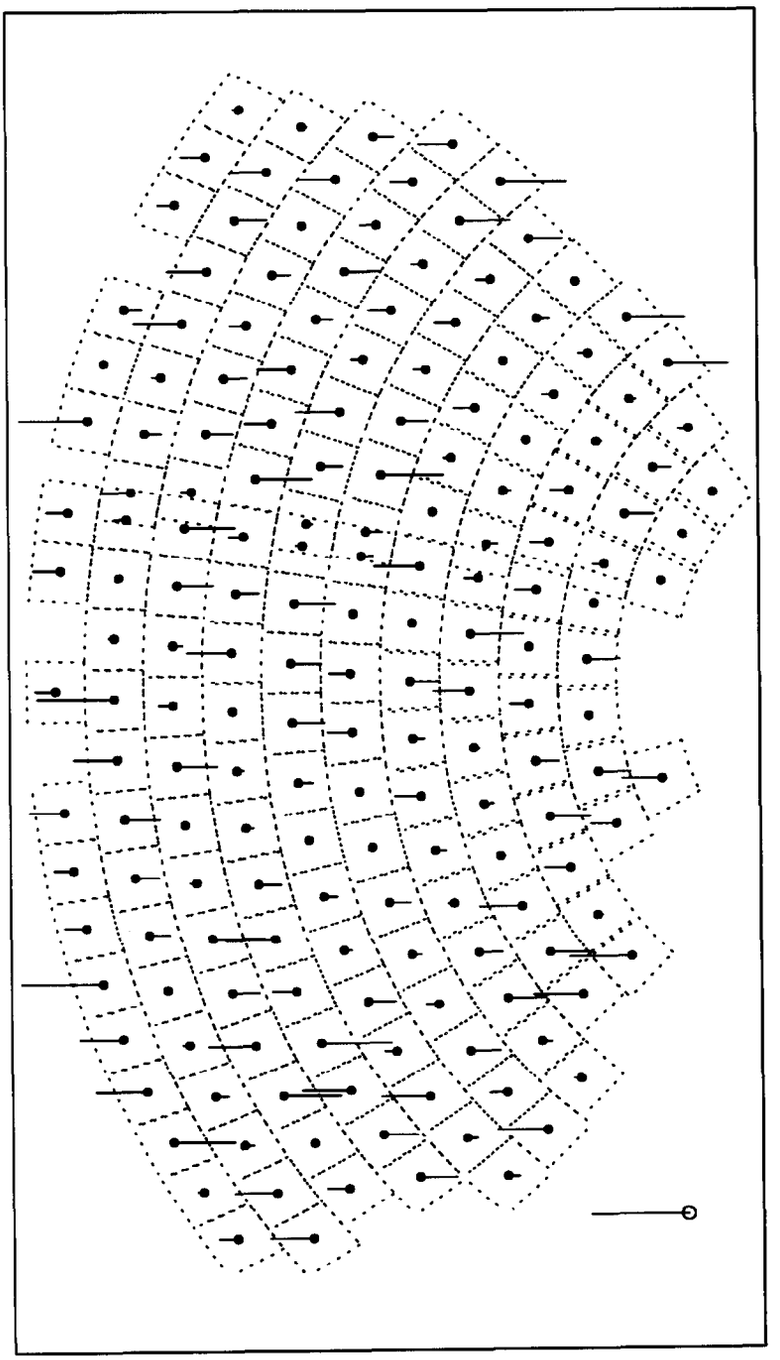

Figure 6:

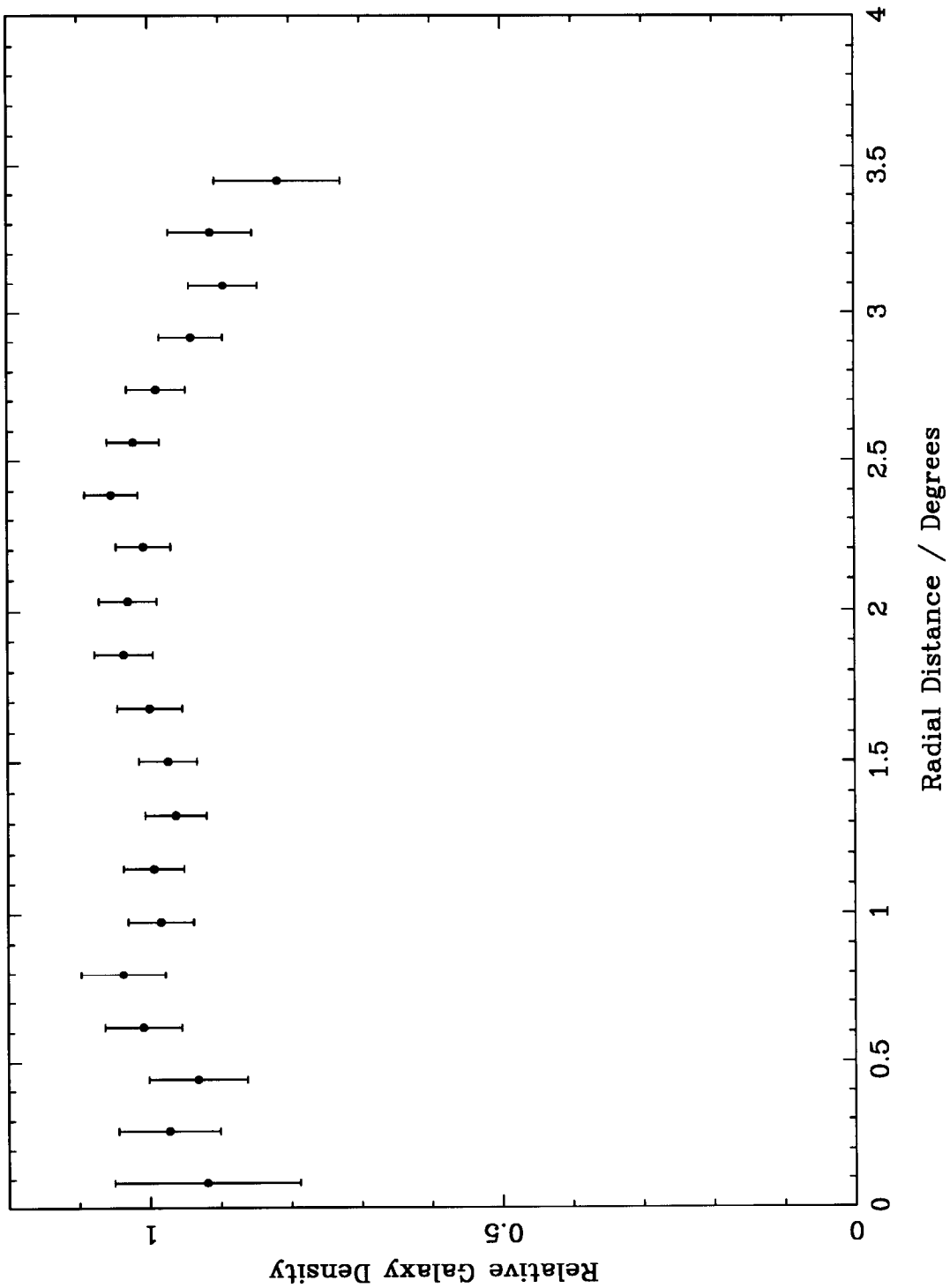
Relative Galaxy Density
0
0.5
1
Radial Distance / Degrees
0
0.5
1
1.5
2
2.5
3
3.5
4

Figure 7:

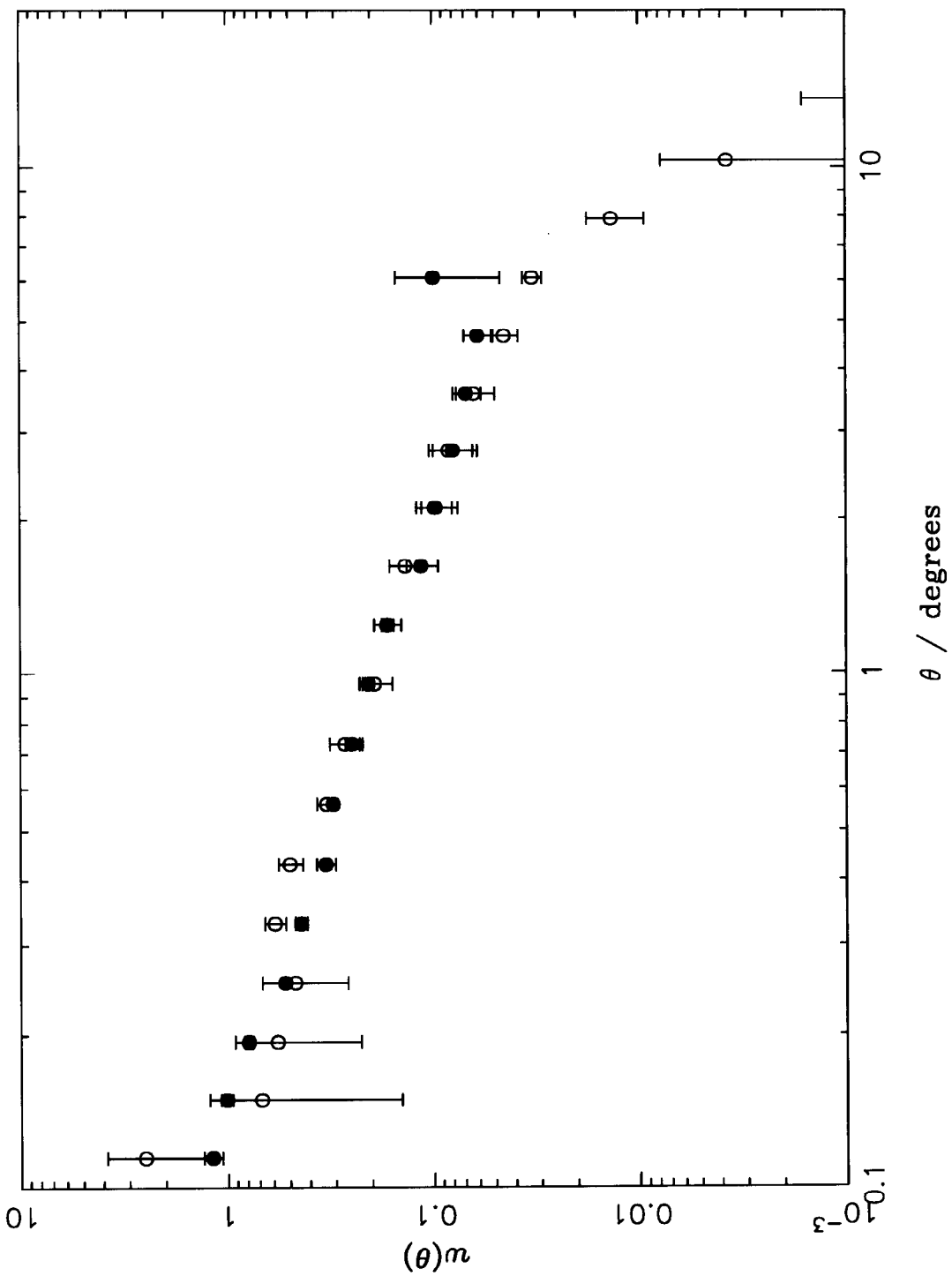

Figure 8:

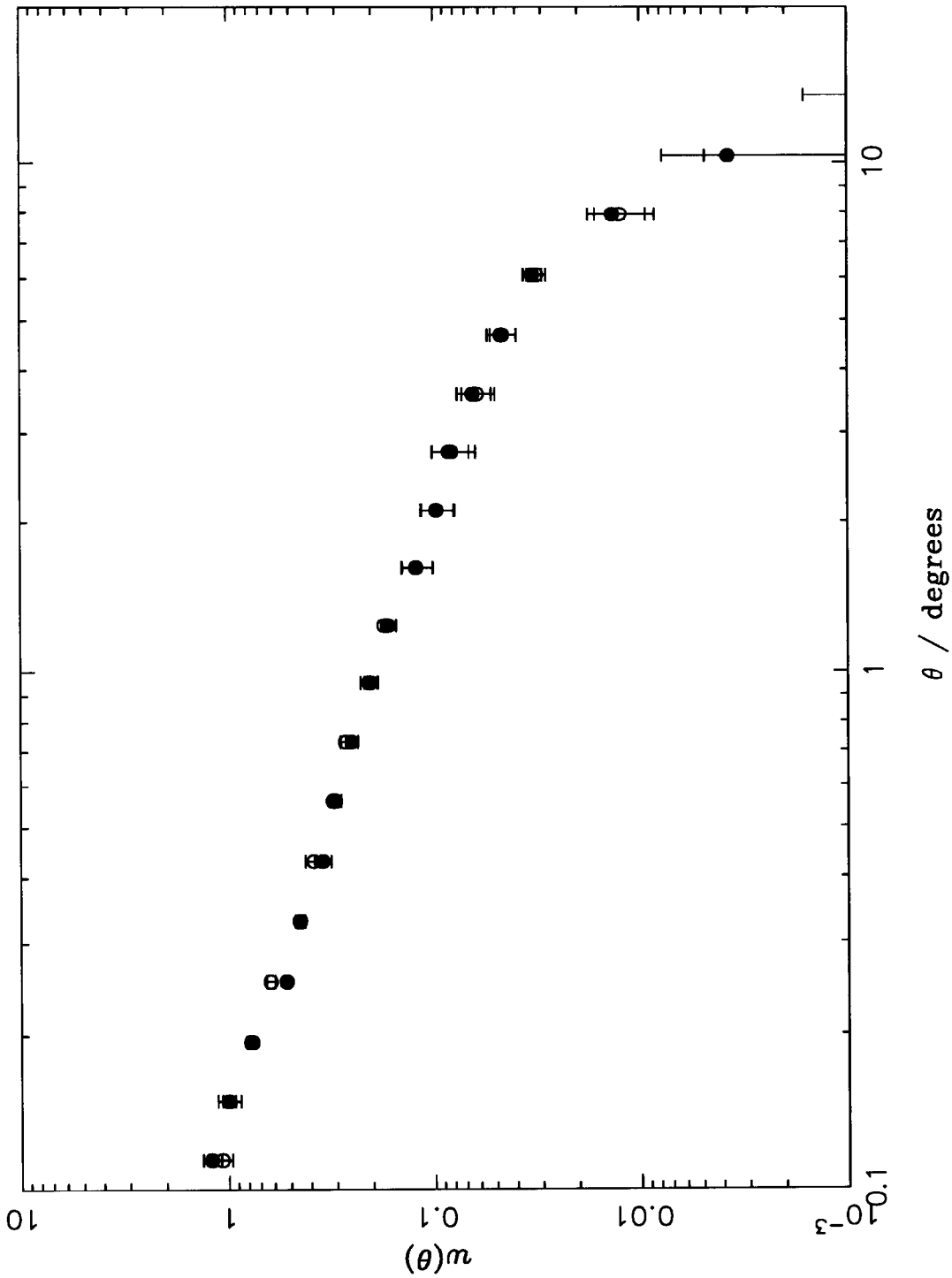

Figure 9:

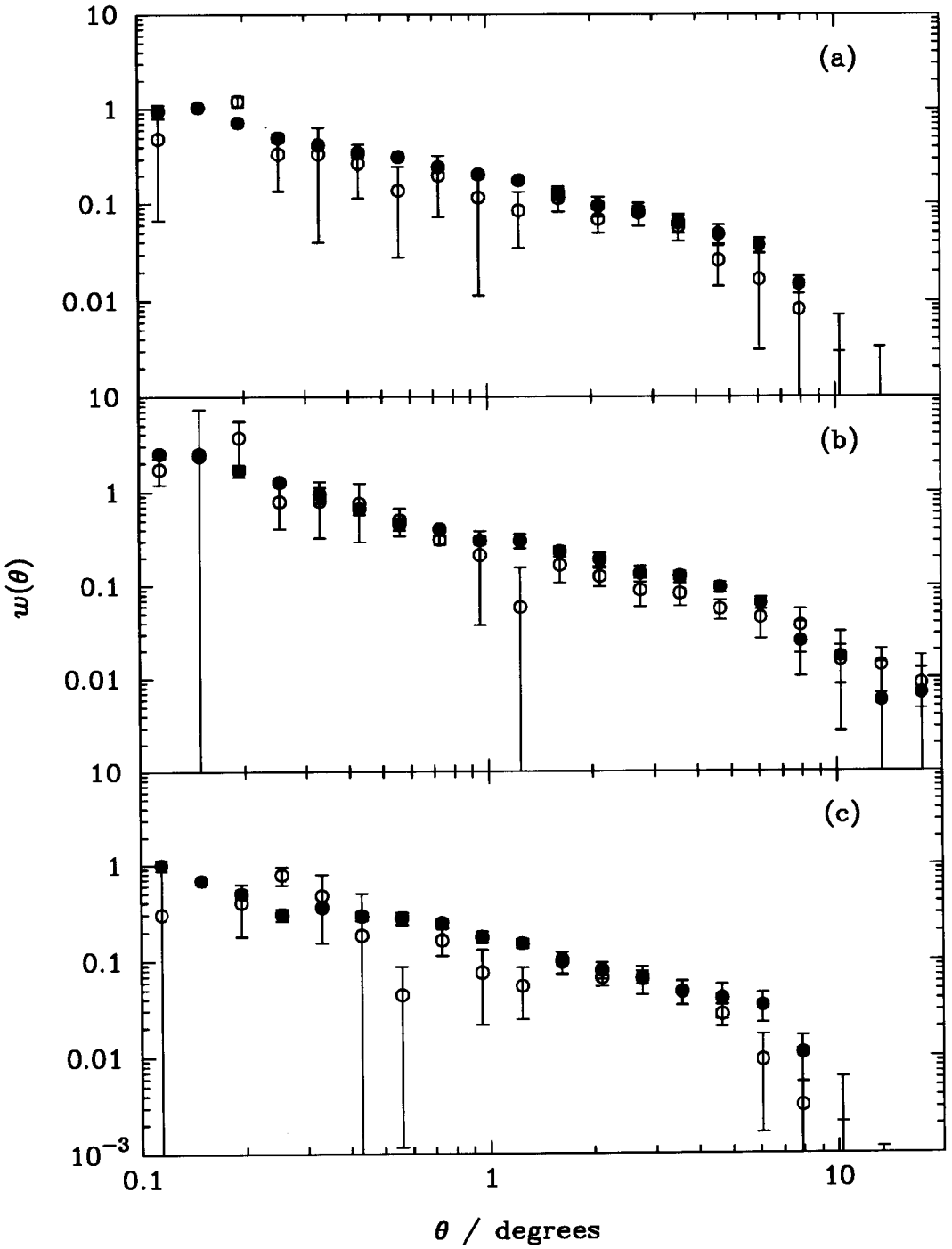

Figure 10:

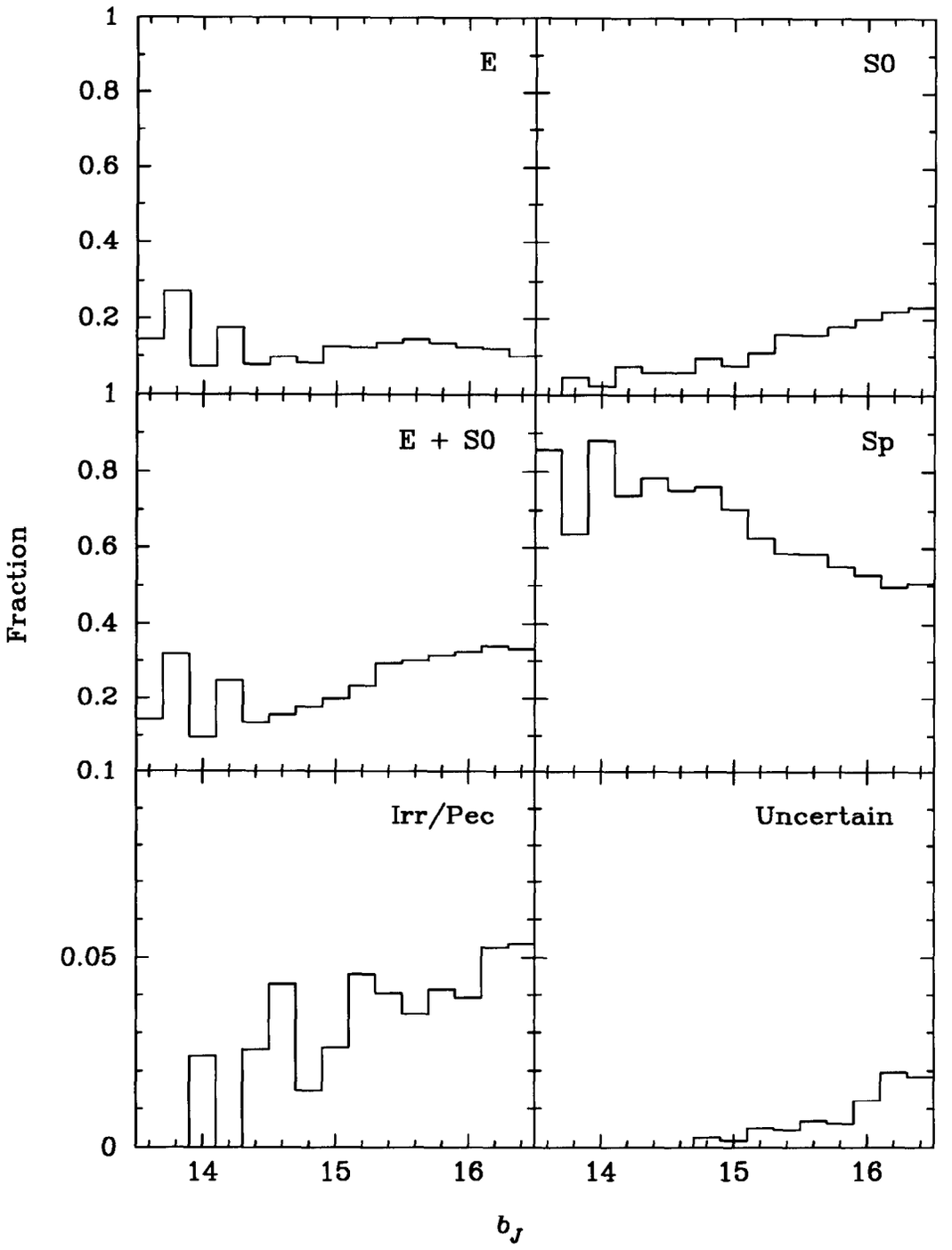
E
S0
E + S0
Sp
Irr/Pec
Uncertain
Fraction
b_J
1
0.8
0.6
0.4
0.2
0.1
0.05
0
14
15
16

Figure 11:

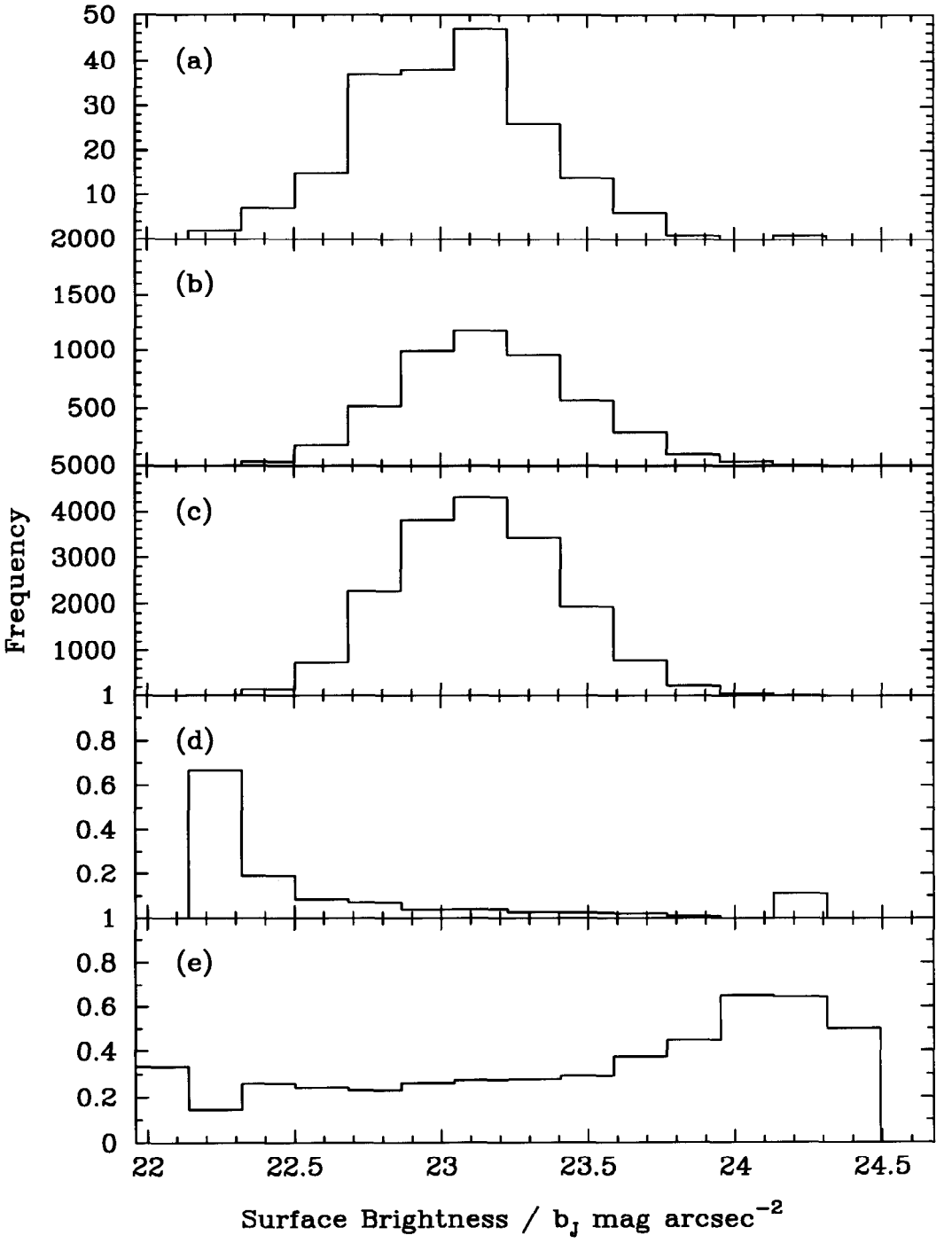
(a)
(b)
(c)
(d)
(e)
Frequency
Surface Brightness / b_J mag arcsec^{-2}
50
40
30
20
10
2000
1500
1000
500
5000
4000
3000
2000
1000
1
0.8
0.6
0.4
0.2
1
0.8
0.6
0.4
0.2
0
22
22.5
23
23.5
24
24.5

Figure 12:

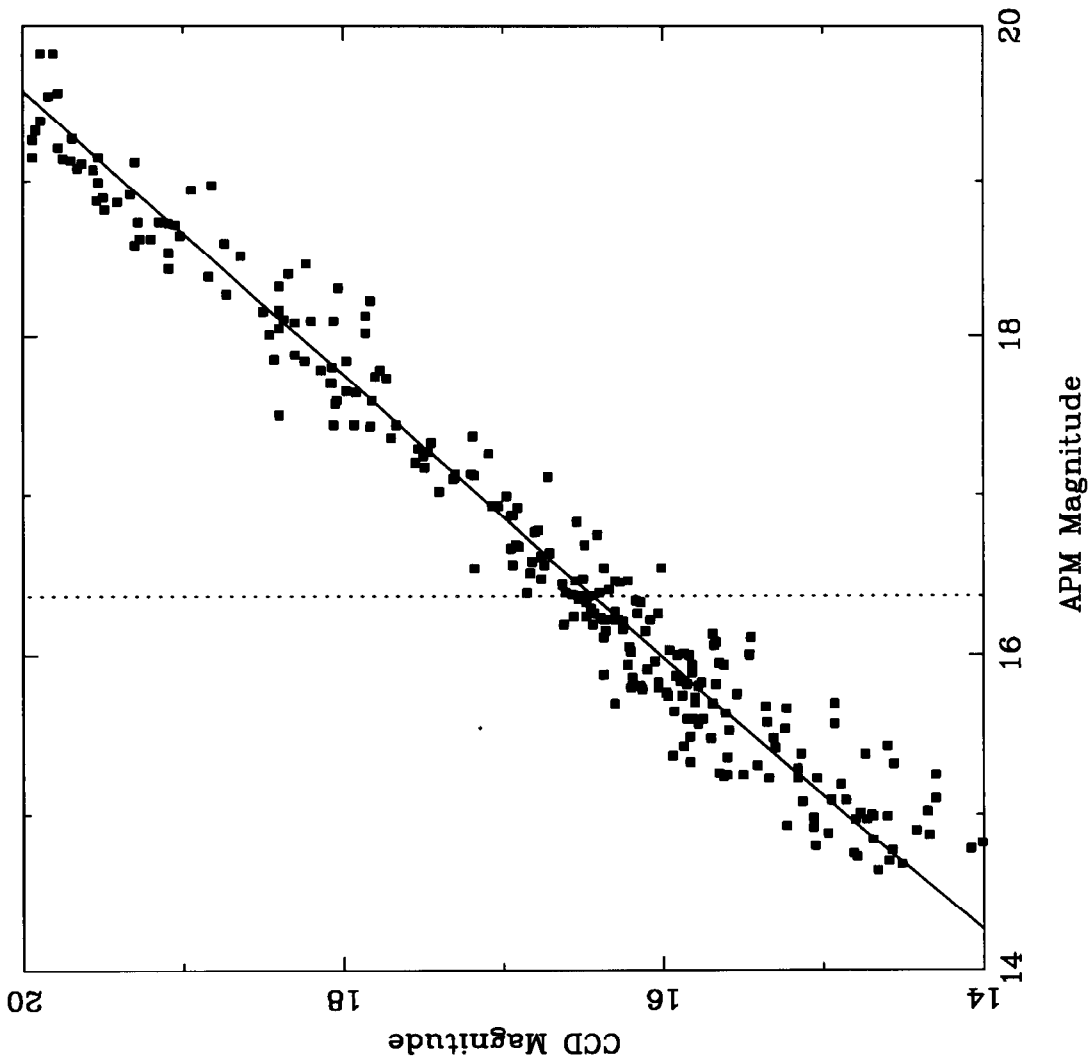

Figure 13:

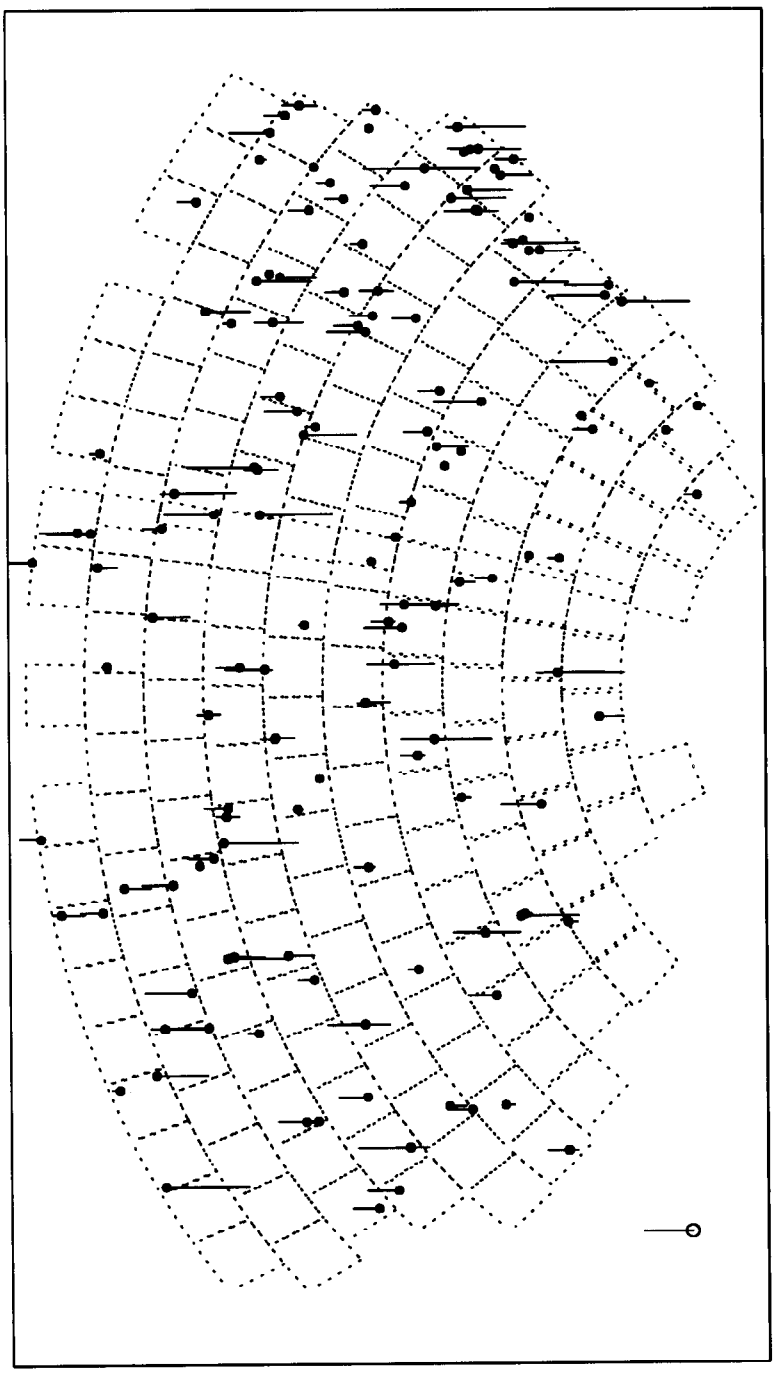

Figure 14:

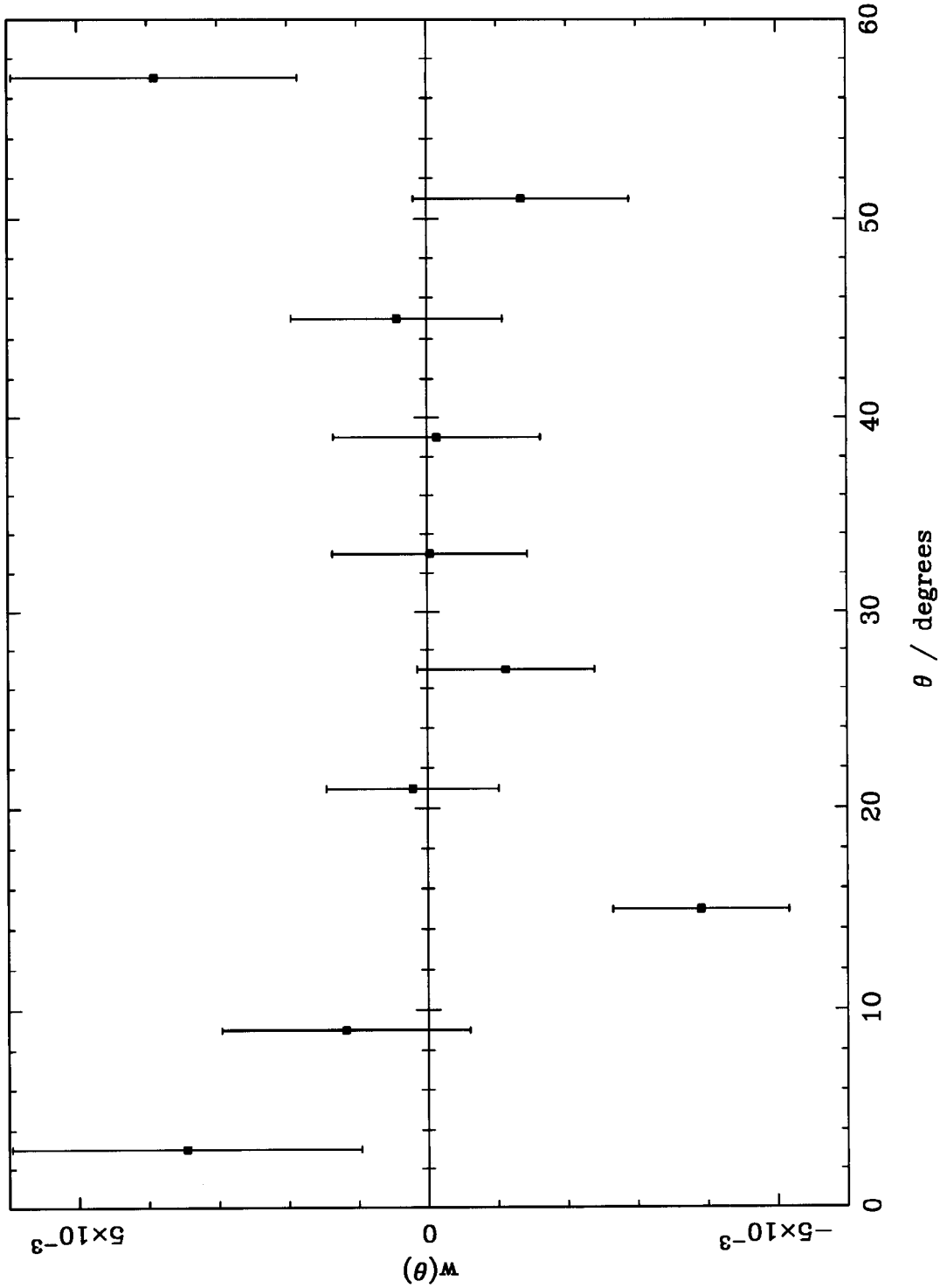

Figure 15:

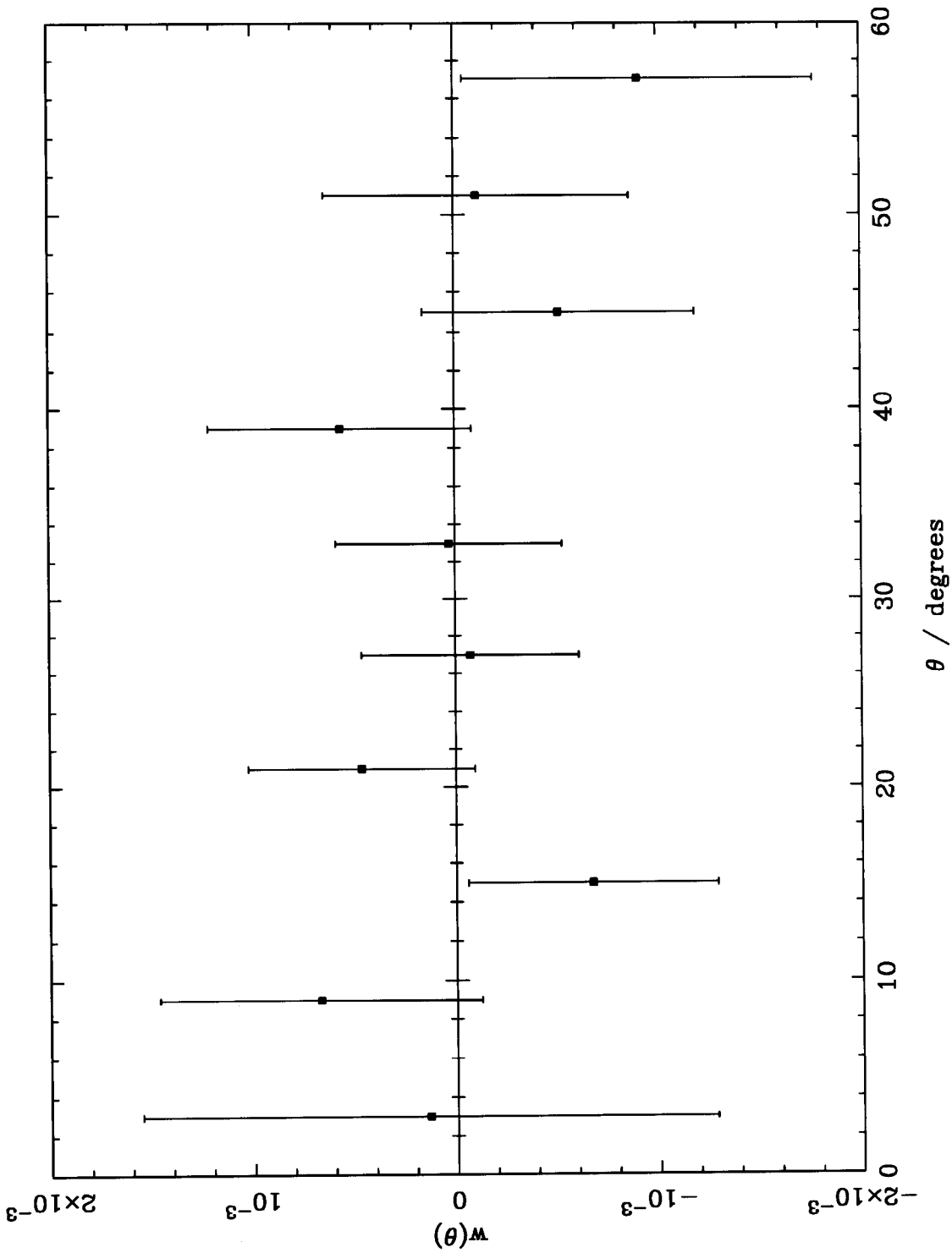

Figure 16:

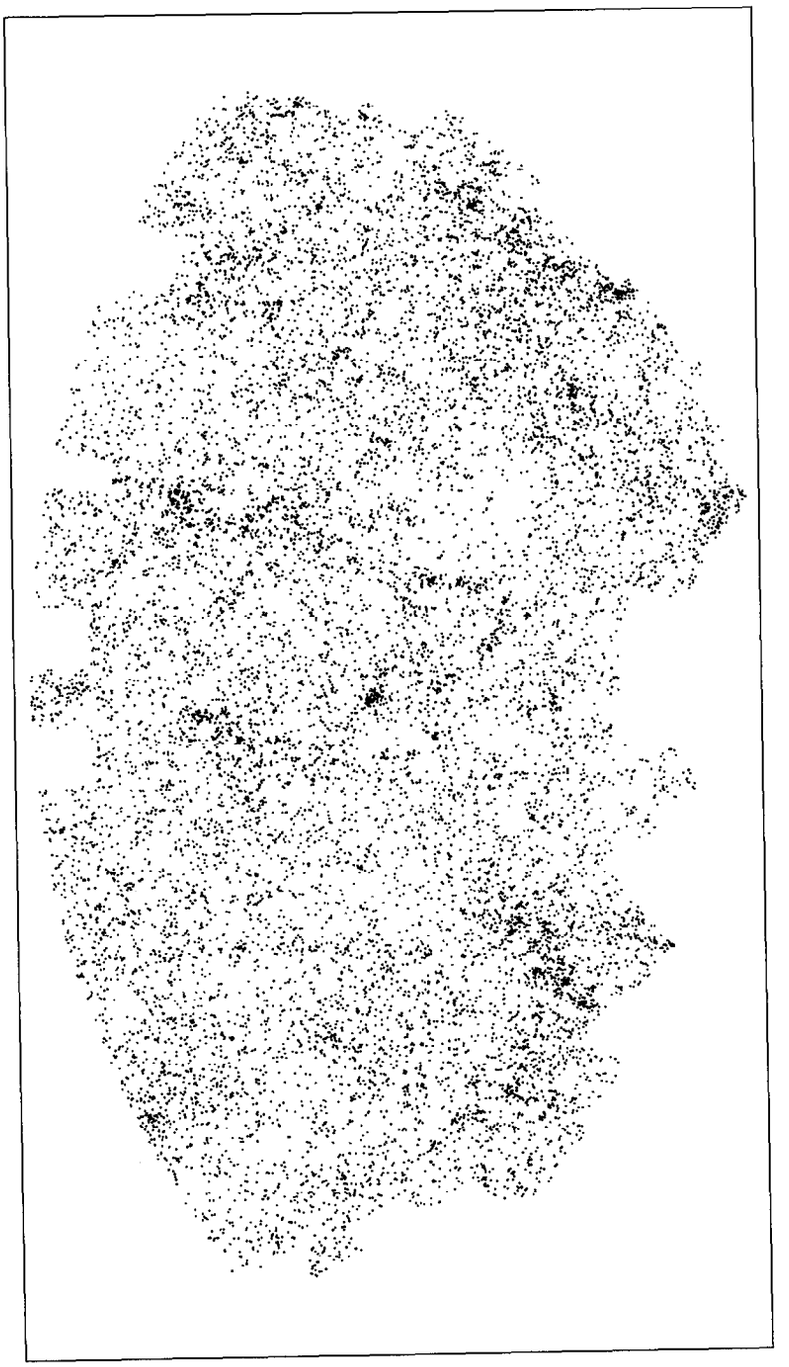

Figure 17:

Figure 18:

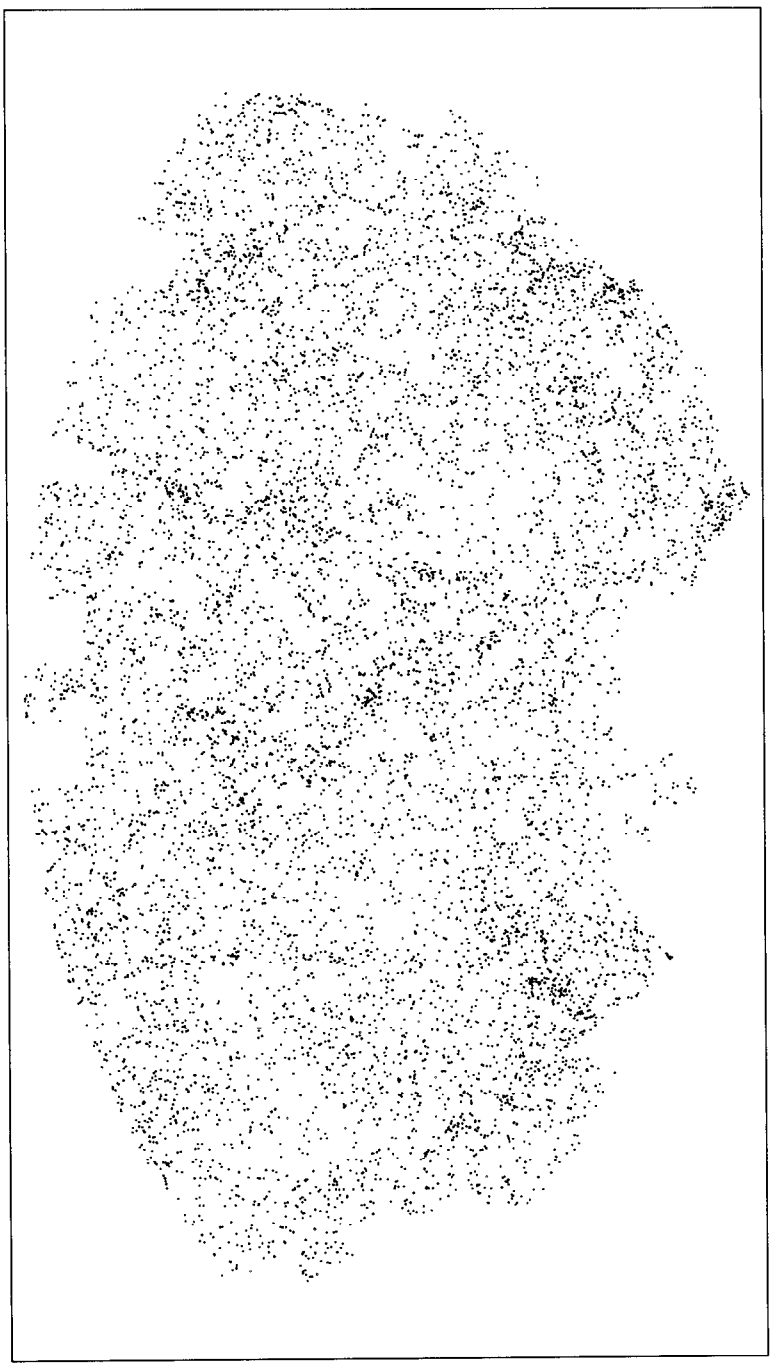

Figure 19:

Figure 20:

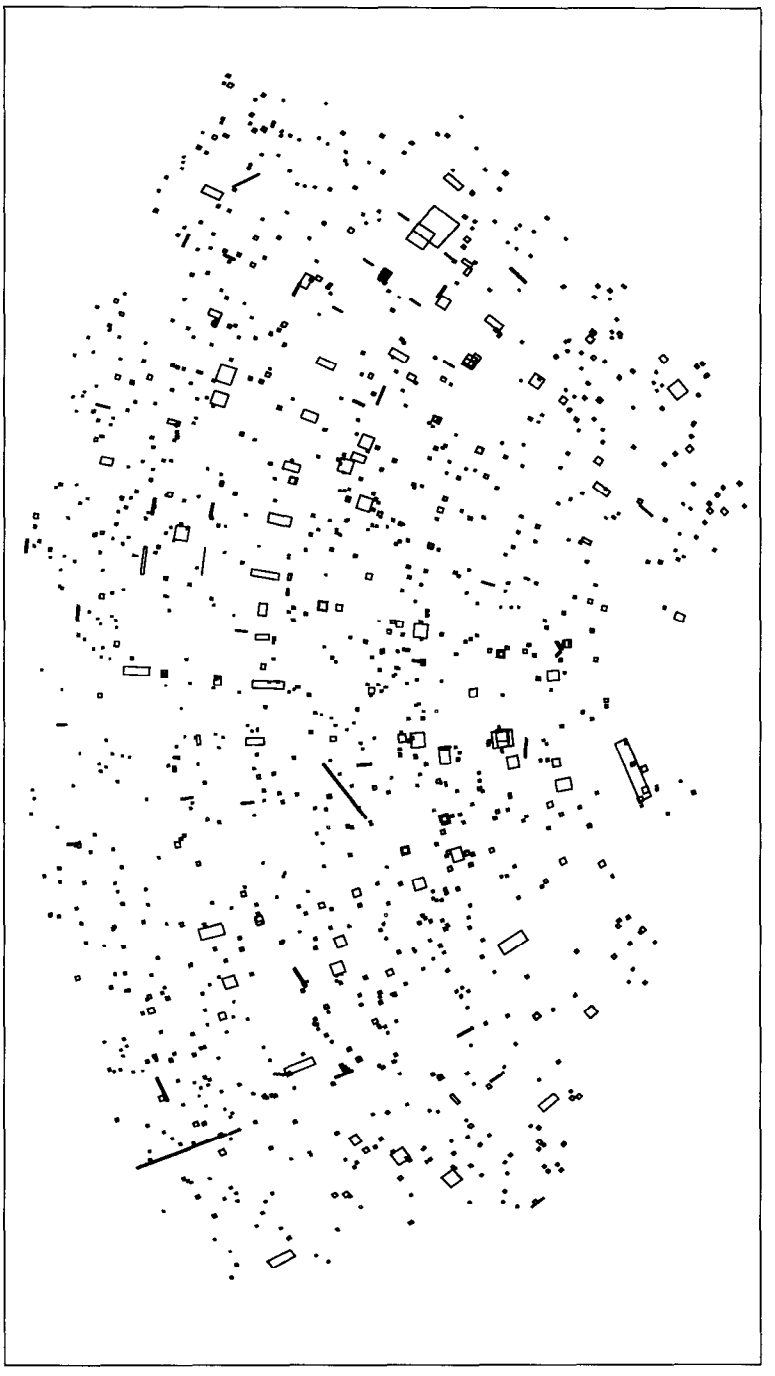

Figure 21:

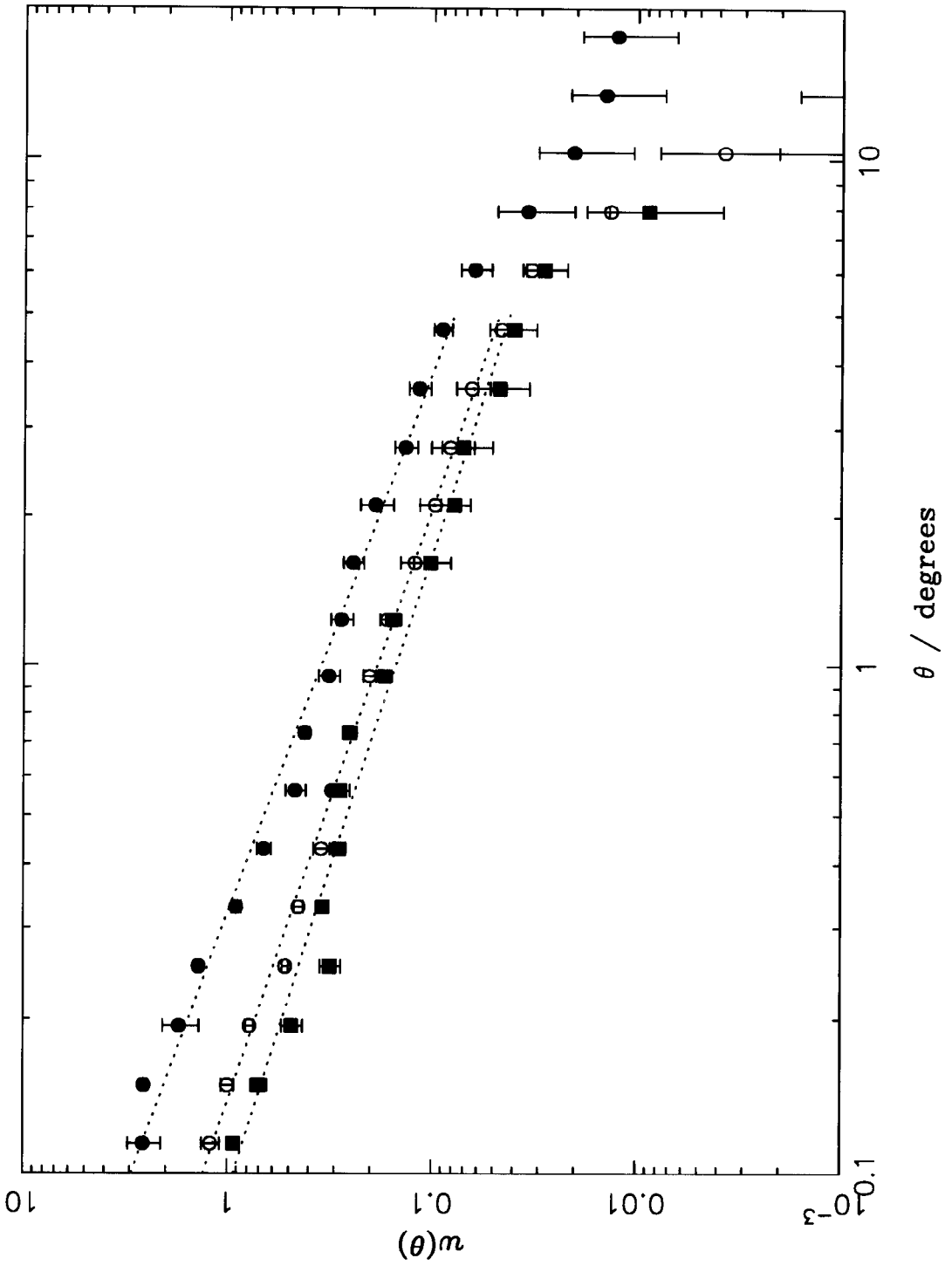

Figure 22: